

Dynamic Elastography of Pre-stressed Material with Multi-Directional Excitation in a Table Top MRI System

BY

FEDERICA DIBENNARDO

B.S, Politecnico di Milano, Milan, Italy, 2021

THESIS

Submitted as partial fulfillment of the requirements
for the degree of Master of Science in Bioengineering
in the Graduate College of the
University of Illinois at Chicago, 2021

Chicago, Illinois

Defense Committee:

Thomas J. Royston, Chair and Advisor

Dieter Klatt

Pasquale Vena, Politecnico di Milano

To my family

ACKNOWLEDGMENTS

Foremost I would like to thank Dr. Thomas J. Royston, who gave me the possibility to stay another semester in Chicago and to work in the Acoustics and Vibration Laboratory, at UIC, exploring the fascinating field of Magnetic Resonance Elastography, through my thesis project. Also thank you to Dr. Pasquale Vena for the help and support in my thesis. I would to thank Dr. Dieter Klatt for helping me during my thesis project.

I am thankful also to Josh for helping me creating the setups and make any adjustments to them, to Martina Guidetti and Shujun Lin that taught me how to use and implement the Table Top System in the laboratory and for being always available and supportive on my work giving me very useful indications.

I would like to thank also Alberto for sharing with me this great opportunity at UIC and for helping me out in everything inside and outside the lab. He was a support and made this experience even more fun and unforgettable.

Special thanks go to my friends in Italy that even though they were not with me in Chicago during my experience, they were always caring and helped me in difficult moments.

A big 'thank you' goes to my brothers, Dario and Luca, for making me laugh and for being caring in their own ways, teaching me to be patient and understanding.

Last, but not least, I am truly grateful to my parents, Ugo and Grazia; for teaching me the meaning of hard work, to never give up, and to believe always in what you are doing. They were continuously there for me and supported me in every big decision; giving me the chance

ACKNOWLEDGMENTS (continued)

to live this wonderful experience in Chicago.

FD

TABLE OF CONTENTS

<u>CHAPTER</u>	<u>PAGE</u>
1 INTRODUCTION	1
2 MAGNETIC RESONANCE ELASTOGRAPHY	5
2.1 MRI physics	6
2.2 Driver Devices	10
2.3 Acquisition of wave images	11
2.4 Mechanical parameters assessment	17
3 PROPAGATION OF WAVES	19
3.1 Body Waves	19
3.2 Linear Elastic Waves	21
3.2.1 Equation of motion for a linear elastic continuum	25
3.3 Torsional and Longitudinal case	30
3.4 Scalar Helmholtz Equation	33
3.4.1 Multiparameter Inversion	37
3.5 Discretization and Noise	39
3.5.1 Equation of motion for skeletal muscle	40
3.6 Viscoelastic models for biological tissue	48
4 STATE OF THE ART	52
4.1 Torsional Actuation experiments	52
4.2 Table Top System	53
4.3 Phantom	54
5 MATERIAL AND METHODS	56
5.1 Preparation of the isotropic phantom	56
5.1.1 Anchor and Endcap	57
5.1.2 Weights	59
5.2 Setup mechanics	59
5.2.1 Actuators	60
5.3 Preliminary testing	61
5.4 Stepper Motor and Piezoelectric setup	63
5.5 Setup with two piezoactuators	64
5.6 MRE computational study	68
6 RESULTS AND DISCUSSION	71
6.1 Examination of motion	71

TABLE OF CONTENTS (continued)

<u>CHAPTER</u>		<u>PAGE</u>
	6.1.1 Axial excitation	72
	6.1.2 Torsional excitation	74
	6.2 MRE experiments	75
	6.2.1 Piezoelectric actuator	75
	6.2.2 Stepper Motor actuator	76
	6.2.2.1 Excitation with prestrains	84
	6.3 COMSOL analysis	87
7	CONCLUSION	93
	APPENDICES	95
	Appendix A	96
	CITED LITERATURE	102
	VITA	107

LIST OF TABLES

<u>TABLE</u>		<u>PAGE</u>
I	Input parameters in COMSOL	69
II	Displacement measured from the results obtained by the <i>Agilent</i> 35670A for 200, 300, 400, 500 Hz using the Piezoelectric.	74
III	Displacement measured from the results obtained by the <i>Agilent</i> 35670A for 200, 300, 400, 500 Hz using the Stepper Motor.	75

LIST OF FIGURES

<u>FIGURE</u>		<u>PAGE</u>
1	Behaviour of spins of the protons: On the left it is shown the case when it is not present an external magnetic field, characterized by a caotic motion. On the right instead, there is the behaviour when there is an external magnetic field H_0 and the spins are aligned to it	7
2	Representation of the two components, \vec{M}_L and \vec{M}_T , that constitute the macroscopic bulk magnetization. In which the absolute value $ \vec{M} $ corresponds to the the magnitude and θ is the phase of the vector. Lecture notes, BioE 594 "Elastography", Instructor: Dieter Klatt, Fall 2020, University of Illinois at Chicago	8
3	Example of a system for MR Elastography in which is analyzed the abdomen. In the top row are represented the hardware elements: far from the magnetic field generated by the MRI scanner is placed the active driver, which is transmitted through a conductive tube to the passive driver placed on the tissue interested. On the left bottom part it is shown where is placed the passive driver and on the right bottom the whole MRE examination set up.	12
4	MRE sequence with the traditional gradient echo sequence with motion-encoding gradient (MEG) applied along the slice selection direction to capture motion in the direction of the through-plane. Lecture notes, BioE 594 "Elastography", Instructor: Dieter Klatt, Fall 2020, University of Illinois at Chicago	13
5	Steps applied in MRE to obtain the wave image. Starting from the application of the 1D Fourier Transform along s to MR signal phase φ , and then scaling with the encoding efficiency ξ	16
6	Description of voxels displacement in the ROI, in which is valid the assumption of intravoxel coherent motion, meaning voxels are characterized by stationary spins.	18
7	Illustration of the consequences of noise and discretization. The graph shows the wave speed (m/S) in relation to the resolution (pixel per wavelength). In the case of low resolution there is an overestimation by discretization and for higher resolution there is an underestimation given by noise	40

LIST OF FIGURES (continued)

<u>FIGURE</u>		<u>PAGE</u>
8	The figure illustrates the basic components of a skeletal muscle. Starting from the external layer, there is: the Epimysium, Perimysium that surrounds the muscle fibers and the Endomysium that covers each muscle fibers. Inside the Endomysium there is the Sarcolemma, which is the cell membrane. Finally inside the Sarcolemma there are Myofibrills that are constituted by two main proteins: Actin and Mysosin.	42
9	In figure (a) is represented the experimental shear waves in the case of agarose. On the left-hand side of (b) and (c) are illustrated the magnitudes of MRE representations. On the right-hand side of (b) and (c) are showed the experimental shear waves in a skeletal muscle of a right arm of the same subject, in sagittal and coronal slice position, respectively.	43
10	Representation of the tendon with actuator at the distal tendon. The image plane coincides with the stress plane, obtaining a planar stress situation. $\mathbf{f} = [f_\rho, f_3]$ is the resulting force vector and	
11	Illustartion of the most used viscoelastic models with the respective value of the complex shear modulus: Maxwell, Voigt, Zener, Jeffreys and fractional Zener. Below that are represented the rheological elements from the spring, dashpot and springpot, a combination between the spring and dashpot.	50
12	Setup composed by Stepper motor, with the black plastic rod, the Vera clear component that connect the coupler to the rod and the acrylic support base	53
13	Diagram of the mold used to create the <i>Ecoflex</i> TM 00-30 phantom. The dark grey component is the Endcap, the grey part is the Anchor and in yellow is represented the Ecoflex phantom, which is placed inside the mold.	56
14	3D illustration of the weigth anchor.	58
15	3D illustration of the Mold Endcap	58
16	Lead bullet weights used in the setup.	59
17	Reference system in the Table Top MRI Scanner.	60
18	3D illustration of the 3D stepper Motor adapter.	61

LIST OF FIGURES (continued)

<u>FIGURE</u>		<u>PAGE</u>
19	Representation of the Stepper Motor setup with the sample.	62
20	Illustration of the new design of the phantom, realized with the new adapter.	63
21	Stepper Motor actuator 14HS13 – 0804S with the respecting acrylic structure. On the left is showed the top view and on the right side the front view.	65
22	Piezoelectric actuator PAHL60/20 with the respecting acrylic structure. On the left is showed the top view and on the right side the front view.	65
23	Top view and front view of the setup with two piezoactators.	65
24	Representation in 3D of the holder component on the right. On the left it is illustrated the top view of it, with the respective measurements	67
25	Phantom with the new adapter.	67
26	Representation of the <i>Polytec PDV – 100</i> Portable Digital Vibrometer.	71
27	Representation of displacement and frequency values using <i>Agilent 35670A</i>	73
28	On the left is showed the real (top) and imaginary (bottom) part; on the right the absolute (top) and the phase (bottom) values of the complex wave image for 200Hz.	76
29	Waves images for 200Hz. On the left, top row: real part and top bottom: Imaginary part. On the right, top row: absolute values and top bottom: phase values	77
30	Waves images for 400Hz. On the left, top row: real part and top bottom: Imaginary part. On the right, top row: absolute values and top bottom: phase values	77
31	Waves images for 600Hz. On the left, top row: real part and top bottom: Imaginary part. On the right, top row: absolute values and top bottom: phase values	78
32	Waves images for 800Hz. On the left, top row: real part and top bottom: Imaginary part. On the right, top row: absolute values and top bottom: phase values	78

LIST OF FIGURES (continued)

<u>FIGURE</u>		<u>PAGE</u>
33	Waves images for 1000Hz. On the left, top row: real part and top bottom: Imaginary part. On the right, top row: absolute values and top bottom: phase values	79
34	Magnitude images for each time steps at 400Hz.	80
35	Phase images for each time steps at 400Hz.	81
36	Magnitude images for each time steps at 600Hz.	81
37	Phase images for each time steps at 600Hz.	82
38	Stepper Motor Setup with the weights for a 10% prestrain.	84
39	Waves images for 400Hz. On the left, top row: real part and top bottom: Imaginary part. On the right, top row: absolute values and top bottom: phase values	85
40	Waves images for 800Hz. On the left, top row: real part and top bottom: Imaginary part. On the right, top row: absolute values and top bottom: phase values	85
41	Waves images for 400Hz. On the left, top row: real part and top bottom: Imaginary part. On the right, top row: absolute values and top bottom: phase values	86
42	Waves images for 800Hz. On the left, top row: real part and top bottom: Imaginary part. On the right, top row: absolute values and top bottom: phase values	86
43	From the left to the right: axial slices in the x-direction of wave images for 0%, 10% and 20% elongation for 400Hz.	88
44	From the left to the right: axial slices in the z-direction of wave images for 0%, 10% and 20% elongation for 400Hz.	88
45	From the left to the right: axial slices in the z-direction of wave images for 0%, 10% and 20% elongation for 400Hz.	89
46	From the left to the right: axial slices in the z-direction of wave images for 0%, 10% and 20% elongation for 400Hz.	89
47	From the left to the right: axial slices in the x-direction of wave images for 0%, 10% and 20% elongation for 400Hz.	90

LIST OF FIGURES (continued)

<u>FIGURE</u>		<u>PAGE</u>
48	From the left to the right: sagittal slices in the x-direction of wave images for 0%, 10% and 20% elongation for 400Hz.	91
49	From the left to the right: axial slices in the z-direction of wave images for 0%, 10% and 20% elongation for 400Hz.	91
50	From the left to the right: sagittal slices in the z-direction of wave images for 0%, 10% and 20% elongation for 400Hz.	92
51	Datasheet of the Piezoelectric actuator 60/20	97
52	Datasheet of the Stepper Motor 14HS13-0804S	98
53	Datasheet of the Piezoelectric P842.10	99
54	Technical Drawing of the Piezoelectric P842.10	100
55	Datasheet and technical drawing of the flexible tip P176.50	101

LIST OF ABBREVIATIONS

AIDE	Algebraic inversion of the differential equation
TE	Echo Time
FEA	Finite Elements Analysis
FEM	Finite Element Method
GPA	Gradient Power Amplifier
MR	Magnetic Resonance
MRE	Magnetic Resonance Elastography
MRI	Magnetic Resonance Imaging
MEG	Motion Encoding Gradient
PDE	Partial Differential Equation
RF	Radio Frequency
ROI	Region Of Interest
TR	Repetition Time
SLDV	Scanning Laser Doppler Vibrometry
SE	Spin Echo

SUMMARY

There is a significant correlation between changes in mechanical properties and disease or injuries. For this reason were developed techniques, such as biopsy and manual palpation, to detect tissue's mechanical structure.

These latter techniques are characterized by a lot of disadvantages. For instance, a biopsy is invasive and not reliable, and manual palpation is qualitative, superficial, and operator dependent.

As a consequence of these drawbacks, two non-invasive techniques were developed: Ultrasound Elastography and Magnetic Resonance Elastography.

This work is based on Magnetic Resonance Elastography, which can provide motion encoding simultaneously in three directions, is not depth-limited and provides a good resolution. This imaging technique utilizes standard MRI equipment and equipment and an actuator to generate vibrations transmitted to the analyzed tissue.

In a method developed by researchers at UIC a decade ago, high frequency vibratory shear waves are induced and imaged in a small sample within a test tube by axially driving the test tube in the MRI system. This motion of the test tube, using a piezoelectric actuator, results in radially converging (geometrically focused) axially-polarized shear wave motion within the sample. More recently, using the same setup with a sample in the test tube, torsional vibratory motion has been induced in the test tube using a stepper motor, in order to drive torsionally-

SUMMARY (continued)

polarized geometrically focused shear waves, which when compared to axially-polarized waves in the same sample, may elucidate its anisotropy.

In the present study, two innovations to this setup are considered. (1) In order to extend the frequency range of the torsional approach, which in turn improves its resolution, the stepper motor is replaced with two piezoelectric actuators that are configured in a way to induce torsional motion. (2) In order to investigate the effect of tensile pre-stress on shear wave motion in a sample, a new arrangement is designed, whereby the test tube is removed and the cylindrically-shaped sample hangs freely in the MRI and can be subjected to different known axial tensile pre-stresses while simultaneously performing MRE studies using both axially-polarized and torsionally-polarized shear waves. The measurements obtained using MRE are wave images representing the displacement field in cross-sectional and sagittal slices within an isotropic cylindrical phantom under different pre-stresses. Experimental measurements are compared to computer simulations of the experiment using finite element analysis (FEA).

CHAPTER 1

INTRODUCTION

Traditionally, to evaluate diseases physicians take advantage of the four senses: hearing, sound or auscultation, visual perception, smell or olfaction, and manual palpation.

In particular, manual palpation is a useful method to assess biological tissue. Indeed, by the sense of touch physicians can estimate qualitatively the response to deformation of the tissue that is evaluated, since mechanical properties of tissues are different among physiological and pathological conditions [1].

Even though this is a powerful method, it is restricted to the body surface; hence the location of pathologies inside the body cannot be located. Besides, this technique is characterized by intraobserver and interobserver variability.

The gold standard to determine hepatic fibrosis grade is liver biopsy. This method is a procedure characterized by the removal of a small piece of liver tissue, so it is analyzed under a microscope for signs of damage or disease [2]. In particular, the stiffer is the liver, the higher is the grade of fibrosis; on the other hand, a less stiff tissue represents a better condition of the liver.

Liver biopsy is characterized by sampling errors given by the small size of the hepatic samples and the non-homogeneity of liver fibrosis. Other limits of this technique are the intraobserver variability and the risk for the patient since it can cause pain, making the subject uncomfortable. Moreover, after the biopsy can occur bleeding and some bacteria might penetrate the

abdominal cavity leading to infection [2].

The method's limitations mentioned have led to the development of different methods such as Elastography.

Elastography is a non-invasive and quantitative remote palpation technique, it is very sensitive to pathological changes since it can evaluate stiffness deep inside the tissue. Therefore the mechanical properties of biological tissue are a fundamental aspect for diagnosis. In the case of elastography, the main approaches to provide imaging of the mechanical properties are ultrasound elastography and magnetic resonance elastography (MRE).

Ultrasound Elastography is not expensive and is versatile. This method works by combining traditional ultrasound technique with mechanical vibration to the tissue examined, such that stiffness can be assessed.

Regarding the measured physical quantity, this method can be divided into strain imaging and shear wave imaging [3]. In the first category, the normal strain is evaluated by applying normal stress to the tissue. Instead, in shear wave imaging is used a mechanical vibrating device to apply dynamic stress to the tissue considered. In this way, the shear wave speed and shear modulus are measured [3].

MRE is a dynamic and quantitative imaging technique that evaluates the shear modulus (stiffness) of biological tissues through the analysis of mechanical waves with a particular magnetic resonance technique [1]. Exploiting harmonic mechanical excitation shear waves are created; thus, they propagate in-depth in the biological tissue, and the shear modulus of tissue is estimated.

Moreover, knowing that the stiffness is a function of density and the mechanical wave speed; the stiffer is the material, the larger is the wavelength, hence the faster is the velocity of propagation of the wave through the tissue.

In this work is used a Benchtop MRI system found in the Motion Encoding Laboratory at UIC, composed by different components that will be described in details later on. This system gives the opportunity to examine in a non-destructive way biological samples.

The Table Top system is then integrated with one new set up that analyzed the vibrational torsion and other two set ups.

The aim of the following work is to develop a new setup in which an isotropic phantom is directly attached to the setup considered. In this case is not present a traditional test tube, but there is a system through which the sample does not require the test tube. The purpose of doing so is then to have the possibility to hang, directly to the phantom, different weights, being able then to analyze the sample's mechanical behaviour at different pre-strain values through Magnetic Resonance Elastography. The innovation of the sample it is investigated by implementing both axial and torsional excitation.

This research study is focused better on torsional vibration, exploiting a Stepper Motor setup. It was also developed a new setup, composed of two piezoelectric actuators placed in counter-phase, with the objective to cross validate vibration on the torsional direction and understand if it is more efficient than the Stepper Motor in causing a displacement on the phantom.

Finally, the different systems are validated to understand if it reasonable to obtain informa-

tion about the mechanical behaviour of the phantom through the Table Top System, when the phantom is at rest and when is elongated.

CHAPTER 2

MAGNETIC RESONANCE ELASTOGRAPHY

MRE is an effective method able to analyze quantitatively the image of mechanical properties of many tissues. The first successful clinical application of MRE is the assessment of liver fibrosis; but other tissues can be examined like the brain, lungs, pancreas and kidneys [4]. This method is precise, it does not depend on the operator and it has the ability to obtain information about tissues that are not reachable by touch.

MRE is a phase-contrast MRI technique capable to develop quantitative maps depicting the mechanical properties of biological tissues [1]. The main steps of MRE techniques are, the application of a harmonic force to the tissue; measurement of the resulting internal displacements of the tissue and lastly, determining the viscoelastic properties of the biological tissue by solving the equation of motion that replicate the behaviour of the tissue of interest. Depending on the tissue that needs to be analyzed the set up changes.

For instance, in a conventional MRE experiment in the human brain, the experimental setup is composed of the scanner, an operating console, where it is observed the experiment and an additional hardware that introduce mechanical vibration onto the region of interest of the tissue. The MRI sequence is triggered to a waveform generator, then the oscillations are amplified through an audio amplifier and later they are transferred to a vibration generator, such that

the vibration is transmitted to the region of interest [5].

2.1 MRI physics

It is important to underline what are the main basics that characterize MR physics. Magnetic Resonance Imaging is a non-invasive imaging technique that can be used to evaluate soft tissues of the body, like the brain, spinal cord and liver. The technique is based on the interaction between an external magnetic field and nuclei.

The human body is mostly composed of water molecules, consisting of hydrogen and oxygen atoms. These atoms are characterized by protons that possess a spin which involves a magnetic moment meaning that each spin can be taken as a mini magnet.

Supposing that there is not an external magnetic field applied to the system the spins of the protons are subjected to a random motion (Figure 1), which means that the sum of the microscopic magnetic moment vectors, the so called macroscopic bulk magnetization, is null [6].

The macroscopic bulk magnetization \vec{M} is constituted by a longitudinal and transverse component. In the case of thermal equilibrium, the overall magnetization corresponds to the longitudinal magnetization, which is parallel to the static magnetic field \vec{B}_0 , while the transverse component is equal to zero [7]. Since in MRI technique is evaluated the transverse component of the macroscopic bulk magnetization it is essential to apply an RF-pulse with the Larmor frequency, which is:

$$\omega = \gamma B_0 \tag{2.1}$$

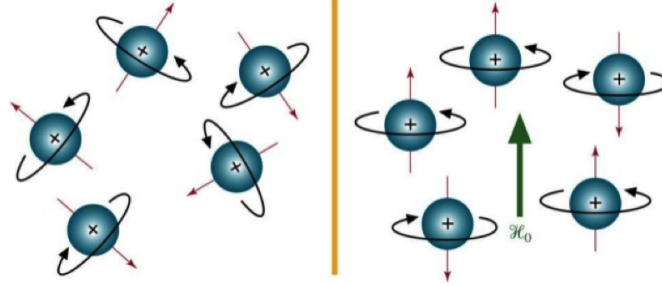


Figure 1: Behaviour of spins of the protons: On the left it is shown the case when it is not present an external magnetic field, characterized by a caotic motion. On the right instead, there is the behaviour when there is an external magnetic field H_0 and the spins are aligned to it

where γ is the gyromagnetic ratio, a constant identified by spinning subatomic particles and in the case of the proton of hydrogen is equal to $2\pi 42.58$ MHz/T.

The condition for exciting transverse magnetization in a slice is called, resonance condition:

$$\omega_{RF} = \omega = \gamma B_0 \quad (2.2)$$

Once the RF-pulse is applied the macroscopical magnetization tilts such that the two components of the bulk magnetization are generated [8]. In particular, the longitudinal component \vec{M}_L is parallel to the z-axis, corresponding to the direction parallel to the magnetic field \vec{B}_0 , the transverse component \vec{M}_T , is parallel to the xy-plane, which is perpendicular to the direction

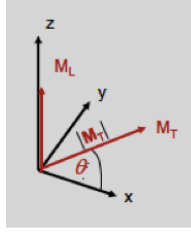


Figure 2: Representation of the two components, \vec{M}_L and \vec{M}_T , that constitute the macroscopic bulk magnetization. In which the absolute value $|\vec{M}|$ corresponds to the the magnitude and θ is the phase of the vector. Lecture notes, BioE 594 "Elastography", Instructor: Dieter Klatt, Fall 2020, University of Illinois at Chicago

of the external magnetic field, as it is shown in Figure 2.

Another important parameter to consider is the angle by which the macroscopical bulk magnetization is tilted when is applied a radiofrequency pulse[9]. This latter component is called 'flip angle' and is equal to:

$$\alpha = \int_0^\tau \Omega_1(t) dt = \gamma \int_0^\tau B_1(t) dt \quad (2.3)$$

In which τ is the duration of the RF-pulse, Ω_1 is the frequency of the RF-pulse and B_1 is the amplitude of RF-pulse. Subsequently, through different relaxation processes the nuclei, that were perturbed due to the introduction of the RF energy, align again and in doing so RF energy is emitted.

The introduction of one single RF-pulse causes the generation of a free induction decay, and with two RF-pulses a spin echo is generated.

In MRI two parameters determine tissue contrast. The first one is the Repetition Time (TR), which corresponds to the time between consecutive pulse sequences implemented to the same slice [10]. The second one is the time corresponding to the moment of measurement of the echo signal given by the spinning protons and it is called Echo Time (TE) [11].

Usually, in MRI there is a 90° -pulse that inclines the spins into the transverse plane, then a 180° -pulse tips over the entire system. There is the possibility to introduce a different combination of angles and RF-pulses, that causes signal dephasing and rephasing in a controlled way.

Human tissue is composed by two relaxation times: T1 and T2. T1 is also called the longitudinal relaxation time and corresponds to the time constant that characterizes the rate at which the excited nuclei return to equilibrium, meaning that the spins realign to the external magnetic field. On the other hand T2, the transverse relaxation time, represents the rate at which nuclei dephase, thus to lose phase coherence among nuclei spinning that are perpendicular to the main field. T2 can be equal or less to T1 since when the return of magnetization to the z-direction occurs, in the xy-plane there is a loss of magnetization.

These two parameters create contrast in MRI images since different tissues relax at different times. For example, fat is composed of hydrogen and carbon and therefore has a short longitudinal relaxation time. Instead, water, which is characterized by hydrogen and oxygen, has a longer T1 than fat due to its high molecular mobility that causes the recovery of the net

magnetization vector to be less efficient [12].

Once the emitted signal is measured, is applied an inverse Fourier transformation that decomposes the MR echo signal and different intensity shades of grey are obtained [10].

2.2 Driver Devices

MRE includes the generation of mechanical vibrations, which are created by the application on the system of external driver devices. To develop an electrical signal is used a signal generator, which is triggered by and coincident to the MR pulse sequence, which is fed into the mechanical driver and then, through an audio amplifier, the MR pulse sequence is increased[1].

MRE actuators differ from the type of vibration source is used to create motion. One of the requirements for these driver systems is to not cause an interaction with the magnetic fields, present in the MRI system.

Another aspect to consider is that the radiofrequency and gradient coils generate time-varying magnetic fields, that could lead to the presence of eddy currents in some electrically conductive components of the transducers. These eddy currents create image artefacts and heat of the transducers.

Typical excitation frequencies used in MRE for clinical applications range from 20 to 100 Hz [13]. Since it is important to guarantee a proper transfer of the wave energy onto the region of interest of the tissue are necessary a high wave amplitudes. Hence, regarding the tissue that is analyzed, the position and the design of the transducers vary.

Different types of driver systems can be utilized and the most common are [1]: an electromechanical driver, which its functioning is based on the Lorentz force; a piezoelectric stack driver system, that exploits the piezoelectric property of a specific material. And lastly, there is the application of an acoustic speaker, which uses the motion of voice coils to create motion. The vibrations are generated by the Lorentz force and the static magnetic field is generated from a magnet placed in the acoustic speaker. For this reason, the speakers must be located outside the main MR magnet, inducing the use of a supplementary component, called passive driver. Because of it, the vibrations generated by the speakers to the region of interest of the tissue are coupled [14][1] (Figure 3).

In general in clinical MRE, the set up and the driver system has to be easy to control by physicians, should not cause any harm to the operator and must be characterized by patient comfort.

2.3 Acquisition of wave images

MRE is based on encoding information on coherent tissue vibration into the phase of MRI signal. Thus MRE sequence diagram is composed by the typical MRI sequence, characterized by a radio frequency pulse waveform, slice-selection gradient and frequency-encoding gradient. Aside from the MRI sequence, it is composed by two more components, one indicates the vibration that causes the vibration generator and the second one is an additional gradient, called Motion Encoding Gradient (MEG) (Figure 4).

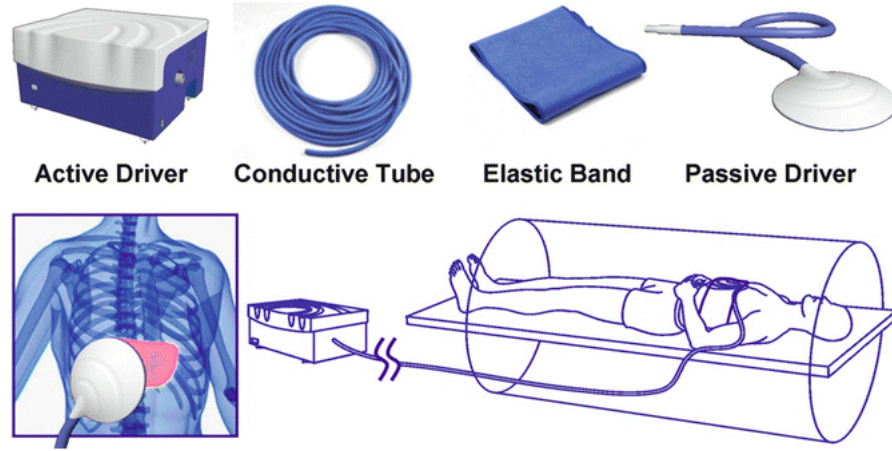


Figure 3: Example of a system for MR Elastography in which is analyzed the abdomen. In the top row are represented the hardware elements: far from the magnetic field generated by the MRI scanner is placed the active driver, which is transmitted through a conductive tube to the passive driver placed on the tissue interested. On the left bottom part it is shown where is placed the passive driver and on the right bottom the whole MRE examination set up.

MEG is included between excitation and signal read out to encode tissue oscillation into the signal phase. The concept is that the vibration motion is generated by the MR scanner that sends a trigger signal to the vibration generator.

To allow the mechanical wave to propagate into the region of interest, the imaging sequence is begun after a certain delay τ and then a single image is acquired. This process is repeated with different delays such that different wave phases are taken. If N corresponds to the number of wave phases acquired, f is the frequency of the mechanical wave, τ is reduced N times in steps

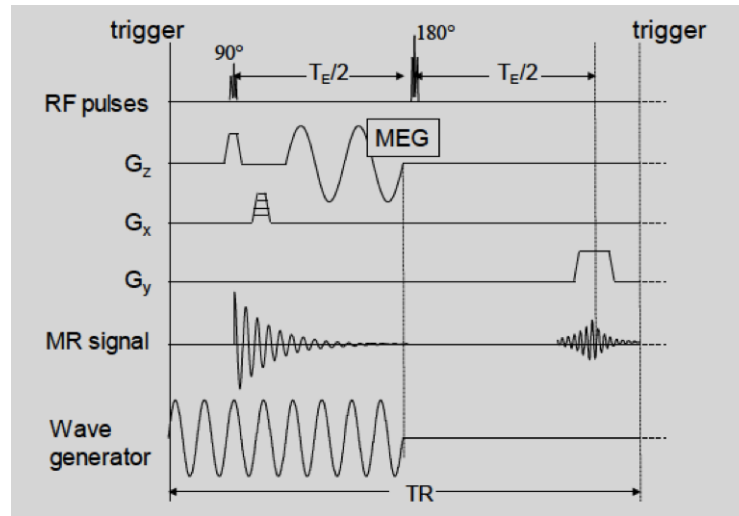


Figure 4: MRE sequence with the traditional gradient echo sequence with motion-encoding gradient (MEG) applied along the slice selection direction to capture motion in the direction of the through-plane. Lecture notes, BioE 594 "Elastography", Instructor: Dieter Klatt, Fall 2020, University of Illinois at Chicago

of $\Delta\tau = \frac{1}{f^*N}$; such that one vibration cycle is sampled with N equidistant data points [13]. τ_k represents the rate of duration of the Motion Encoding Efficiency and can be expressed as:

$$\tau_k = \frac{2\pi q}{\omega_k} \quad (2.4)$$

where q is the MEG number of cycles and ω_k is the angular frequency of MEG. MEG is always bipolar, symmetric and it can be defined as a sinusoidal, step or trapezoidal function.

Furthermore, depending on the direction the gradient can point into any arbitrary direction in

3D space. Thus it is feasible to have access to any vibration direction.

The phase of the transverse macroscopic magnetization is a function of the MEG that starts at time $t = s$:

$$\varphi(s, \vec{r}) = \int_s^{s+\tau} \omega_L(t) dt = \gamma \int_s^{s+\tau} B(t, \vec{r}) dt = \gamma \int_s^{s+\tau} K(t) u(t, \vec{r}) dt \quad (2.5)$$

In which ω_L is the Larmor frequency, γ the gyromagnetic ratio, $B(t, \vec{r})$ is the external magnetic field applied to the system and $K(t)$ is the Motion Encoding Gradient.

In (2.5) is illustrated the magnetic field written as a scalar product of two vectors. The first vector represents the MEG and the second vector describes the vibrational displacement, which is represented as a sinusoidal function and they are written respectively as:

$$K(t) = K_0 \sin \omega_k t + \theta_k \quad (2.6)$$

In which $\theta_k = -\omega_k s$ is the initial condition and as

$$u_n(t) = Y_n \sin \omega_n t + \theta_n \quad (2.7)$$

Where Y_n is the initial amplitude of the displacement and n represents the n^{th} excitation frequency. In the case of multi-frequency signals the displacement u becomes:

$$u(t, \vec{r}) = \sum_n u_n(t, \vec{r}) \quad (2.8)$$

Now, consider to solve the equation 2.5 the phase is equal to:

$$\varphi(s, \vec{r}) = \varphi_n^0 \sin \omega_n s + \theta_n + \Delta\theta_n \quad (2.9)$$

φ_n^0 and ω_n are constant and $\Delta\theta_n$ is space independent representing the phase shift. Considering the sum of the phase corresponding to each frequency the overall MR signal phase is:

$$\varphi(s, \vec{r}) = \sum \varphi_n(s, \vec{r}) \quad (2.10)$$

To obtain the wave image, the encoding efficiency is an important parameter to define. It is proportional to the number of motion encoding gradient cycles and can be seen as the ratio between the amplitude of the MRI signal phase divided by the amplitude of the mechanical

vibration. Therefore, the motion encoding efficiency states with how many radiant one meter of vibration displacement is encoded into the MRI signal phase:

$$\xi_n = \frac{\varphi_n^0}{Y_n} \quad (2.11)$$

Considering now a mechanical wave that is propagating within the sample in a specific direction, the first step to obtain the complex wave image U is to acquire the phase images at different times by introducing a phase offset between MEG and the mechanical vibration. Subsequently, various MR acquisitions are collected and in the case of multifrequency signals a Discrete Fourier Transform is applied along the start time of MEGs.

The Shannon Theorem is applied to evaluate the Nyquist frequency and scaling it with the encoding efficiency [15], the complex wave image is given (Figure 5):

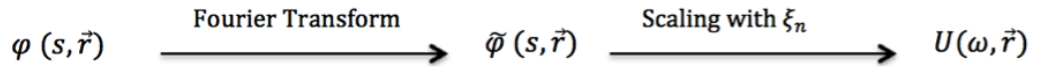


Figure 5: Steps applied in MRE to obtain the wave image. Starting from the application of the 1D Fourier Transform along s to MR signal phase φ , and then scaling with the encoding efficiency ξ .

In MR Imaging, a continuous body is discretized into a set of cubic voxels with finite volumes [13] and each voxel is represented by a contrast-generating physical quantity.

In MRE is assumed intravoxel coherent motion of proton's spins. By introducing a mechanical wave that propagates through the tissue, the single voxel over time oscillates along the direction defined by the polarization of the magnetic wave, but the positions of the individual spins relative to each other are static (Figure 6). Intravoxel spins feature the same precessing macroscopic magnetization within one voxel meaning that they precess coherently.

The displacement of each voxel is given by the phase shift in the MR signal generated by the motion of the individual spins [16]. Since in the shear wave voxels move perpendicular to the direction of the wave propagation, motion encoding gradient is synchronized with the vibration of the actuator, meaning it is possible to read the movement in the MRI phases, where it is considered only the transverse magnetization. Hence MEG can be seen as a snapshot of the mechanical wave and the wave propagation in the tissue can be pictured as wave images, that reflects the displacement of spins.

2.4 Mechanical parameters assessment

The wave images that are estimated could be used as a powerful tool to calculate mechanical properties using mathematical inversion algorithms, described more in details later on [8]. Among the mechanical properties, for clinical application, it is estimated the shear modulus of a medium represented as a complex quantity, in which the real part is the storage modulus and the imaginary part is the loss of modulus that represents the attenuation of the considered

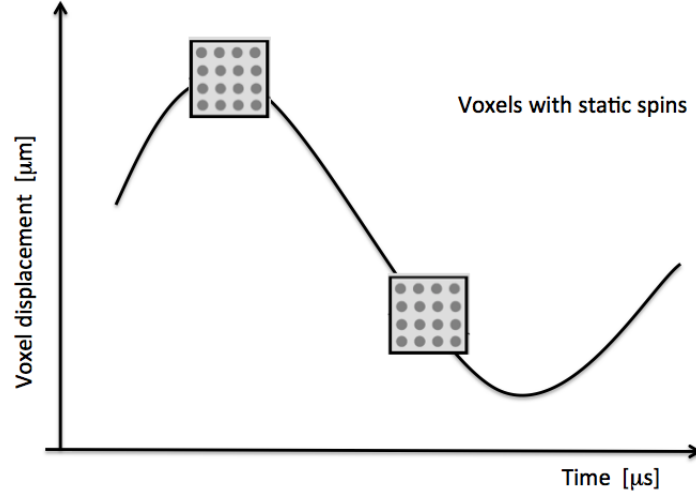


Figure 6: Description of voxels displacement in the ROI, in which is valid the assumption of intravoxel coherent motion, meaning voxels are characterized by stationary spins.

viscoelastic sample[1].

The shear modulus is given by the product between the density (in MRE for a tissue is around 1000 Kg/m^3) and the wave speed. Since the speed wave is the product between the operating frequency and the spatial wavelength of the shear wave, the algorithms are implemented to estimate the wavelength such that the shear modulus can be assessed.

In MRE the result of the mechanical properties of tissue considered are images, called elastograms, that represent both the real and imaginary components of the shear modulus.

CHAPTER 3

PROPAGATION OF WAVES

The following chapter covers how the equation of motion and viscoelastic properties of soft tissues are acquired. First, is gained the wave equation of a linear elastic continuum and afterwards the concept is extended to a transversely isotropic model, that mimics the skeletal muscle.

In nature are present two types of body waves, shear and compression waves. In MRE solely the analysis of shear waves is significant, since compression waves cannot be detected in the ROI of the medium considered.

To obtain the complex shear modulus is applied a Discrete Fourier Transform to the equation of motion, such that mechanical properties are determined.

Additionally, to reproduce the viscoelastic behaviour of the muscle, different viscoelastic models will be explored. Thus, tissue properties are estimated.

3.1 Body Waves

MRE can measure the mechanical properties of the tissue considered, through wave equations, which describe how mechanical waves propagates in the material.

The equation of motion is characterized by different solutions. For this reason, it is necessary to describe the different types of mechanical waves, which differentiate how they propagate

in the solid. There can be found body waves and surface waves [17]. The two most basic types of body waves in a continuum are shear and compression waves.

Compression waves are also called longitudinal waves. Once the wave propagates, the volume of the basic elements changes and the particle displacement is parallel to the direction of propagation. In particular, considering a one-dimensional longitudinal wave that propagates in a tube, the particles oscillate back and forth about their individual equilibrium positions.

In shear waves, while the wave propagates through a medium, the volume elements that compose a wave, do not change. They are also called transverse waves and the particle displacement is perpendicular to the direction of the wave propagation, meaning that, while the wave passes by, the particles oscillate up and down about their individual equilibrium positions.

On the other hand, surface waves are a combination of longitudinal and transverse waves, and in a solid, there are Rayleigh and Love waves [18]. Rayleigh waves are identified by a retrograde elliptical depolarized movement of particles. This implies that the horizontal component of the motion of the particle is in the opposite direction to the propagation direction of the wave. In addition, with the increase of the depth into the solid the wave attenuates very rapidly since the width of the elliptical path decreases.

The Love waves occur when a layer with high density is positioned over a layer with lower density. They oscillate in the left-right direction with regards to the direction of propagation [19]. In biological tissues the wave speed of compression waves is around 1500 m/s and giving its high velocity, its wavelength is longer and faster than shear waves. Indeed, the wave speed in shear waves is slower, around 1-10 m/s, they have a shorter wavelength, and they are more damped

than compression waves. These different characteristics between compression and shear waves underline that just shear waves are relevant in MRE experiments. Differently, compression waves are neglected, due to their high value of wavelength, and therefore they cannot be seen in the region of interest of the soft tissue considered.

3.2 Linear Elastic Waves

The change of body configuration and position is represented by translation, rotation and deformation. In particular, deformation is the only type of change in body configuration that is considered to describe mechanical waves, that propagate through a material. Translation and rotation are not relevant.

This deformation is represented by a tensor, which is symmetric in 3D space and so it has six independent components ($\epsilon_{ij}=\epsilon_{ji}$):

$$\epsilon_{ij} = \begin{pmatrix} \epsilon_{11} & \epsilon_{12} & \epsilon_{13} \\ \epsilon_{12} & \epsilon_{22} & \epsilon_{23} \\ \epsilon_{13} & \epsilon_{23} & \epsilon_{33} \end{pmatrix} = \frac{1}{2} \left(\frac{\partial u_i}{\partial x_j} + \frac{\partial u_j}{\partial x_i} \right) \quad (3.1)$$

The diagonal elements ϵ_{ii} describe the relative change in length in i-direction respectively; instead, the off-diagonal elements ϵ_{ij} define the angle around which i- or j- axis is rotated, and they are also referred as the shear components of displacement.

To determine the quantitative and analytical description of wave equations another parameter has to be taken into account: The stress tensor.

As for the deformation tensor, it has six independent components and it is symmetric ($p_{ij} = p_{ji}$). The stress tensor describes the inner forces inside a body and it is calculated over the matrix product of stress tensor p_{ij} with the surface normal vector n_{ij} :

$$P_j = p_{ij} * n_j \quad (3.2)$$

The relation between the deformation and the stress is governed by the mechanical properties and it is described by the generalized Hook's Law:

$$p_{ij} = f_{ij}(\epsilon_{11}, \epsilon_{12}, \epsilon_{13}, \dots, \epsilon_{33}, T, t, etc.) \quad (3.3)$$

In this matter, each stress tensor component p_{ij} is a function of all strain tensor components ϵ_{ij} , and it could be a function of other parameters such as temperature, time or electric voltage [8].

Since in this case, the body considered is ideal linear elastic there are some assumptions to take into account: Stress tensor depends only on strain tensor components, there is no

deformation when there is no stress and vice versa, small deformations are considered and the relation between stress and strain is linear. Considering these aspects the Hook's Law becomes:

$$P_{ij} = c_{ijkl} * E_{kl} \quad (3.4)$$

Where c_{ijkl} represents a complex 3x3x3 stiffness tensor with 81 components, called Elasticity tensor that relates the tensor of strain with the tensor of stress [20]. Considering that p_{ij} and ϵ_{ij} are both symmetric, the independent components are 36 and accounting for the fact that the elastic deformation energy is conserved, the maximum number of independent components of c_{ijkl} of an anisotropic body becomes 21. Therefore the 4th degree Elasticity tensor can be transformed into a 2nd degree tensor, by using a different matrix notation, such that both strain and stress tensors are converted into vectors: $ij \rightarrow q$ and $kl \rightarrow p$; and thus the Elasticity tensor is symmetric and written as: $c_{ijkl} \rightarrow C_{qp}$.

In the case of an isotropic linear elastic body, the stress-strain relation is:

$$\begin{pmatrix} p_1 \\ p_2 \\ p_3 \\ p_4 \\ p_5 \\ p_6 \end{pmatrix} = \begin{pmatrix} 2\mu + \lambda & \lambda & \lambda & 0 & 0 & 0 \\ \lambda & 2\mu + \lambda & \lambda & 0 & 0 & 0 \\ \lambda & \lambda & 2\mu + \lambda & 0 & 0 & 0 \\ 0 & 0 & 0 & \mu & 0 & 0 \\ 0 & 0 & 0 & 0 & \mu & 0 \\ 0 & 0 & 0 & 0 & 0 & \mu \end{pmatrix} \begin{pmatrix} \epsilon_1 \\ \epsilon_2 \\ \epsilon_3 \\ \epsilon_4 \\ \epsilon_5 \\ \epsilon_6 \end{pmatrix} \quad (3.5)$$

The (3.5) can be written also in in a more compact form by using the index notation:

$$p_{ij} = \lambda \theta \delta_{ij} + 2\mu \epsilon_{ij} \quad (3.6)$$

In which δ_{ij} is the Kronecker delta and equal to:

$$\delta_{ij} = \begin{cases} 1, & \text{if } i = j, \\ 0, & \text{if } i \neq j. \end{cases} \quad (3.7)$$

and $\theta = \epsilon_{ii} = \epsilon_{11} + \epsilon_{22} + \epsilon_{33}$ is the cubic dilatation, which is given by the sum of the diagonal components of the deformation tensor. In the case the material is not compressible, θ is equal to zero and the stress in (3.6) would depend only on the shear modulus μ .

Lastly, from (3.5) and (3.6) is evident that an isotropic linear elastic body depends on only two parameters, the so-called Lamé-constants λ and μ .

3.2.1 Equation of motion for a linear elastic continuum

In a continuum the body forces \vec{F} and the surfaces forces \vec{P} must be in equilibrium:

$$\int_V \vec{F} dv = \int_S \vec{P} ds = 0 \quad (3.8)$$

The relation (3.8) must hold for each component in Cartesian coordinates. Then, by applying the Gauss's law (3.8) is written as:

$$\int_V (F_i + (\nabla * \vec{P})_i) dv = 0 \quad (3.9)$$

And (3.9) must be hold for an arbitrary small volume inside a continuum [21]. Then by using the second Newton's law to express the force, the equation of motion is:

$$\rho \frac{\partial^2 u_i}{\partial t^2} = \frac{\partial p_{ij}}{\partial x_j} \quad (3.10)$$

With p the stress applied on the continuum and x the position in space, the relation (3.10) is valid only considering small deformations.

Including now the assumption of linear stress-strain relation for an isotropic linear elastic body representend in (3.6), the relation in (3.10) becomes:

$$\rho \frac{\partial^2 u_i}{\partial t^2} = \frac{\partial}{\partial x_j} (\lambda \theta \delta_{ij} + 2\mu \epsilon_{ij}) \quad (3.11)$$

Assuming local homogeneity, such that the material properties (λ and μ) do not change in a local small area of the model considered, the equation can be written as:

$$\rho \frac{\partial^2 u_i}{\partial t^2} = \lambda \frac{\partial}{\partial x_i} \theta + 2\mu \frac{\partial}{\partial x_j} \epsilon_{ij} \quad (3.12)$$

Finally, inserting (3.1) in (3.12) the equation of motion is obtained:

$$\rho \frac{\partial^2 u_i}{\partial t^2} = \lambda \frac{\partial}{\partial x_i} \left(\frac{\partial u_1}{\partial x_1} + \frac{\partial u_2}{\partial x_2} + \frac{\partial u_3}{\partial x_3} \right) + \mu \left[\frac{\partial^2 u_i}{\partial x_1^2} + \frac{\partial^2 u_i}{\partial x_2^2} + \frac{\partial^2 u_i}{\partial x_3^2} + \frac{\partial}{\partial x_i} \left(\frac{\partial u_1}{\partial x_1} + \frac{\partial u_2}{\partial x_2} + \frac{\partial u_3}{\partial x_3} \right) \right] \quad (3.13)$$

And (3.13) can be written also in vectorial notation:

$$\rho \frac{\partial^2 \vec{u}}{\partial t^2} = (\lambda + \mu) \nabla \nabla \vec{u} + \mu \nabla^2 \vec{u} \quad (3.14)$$

Where ρ is the mass density (Kg/m^3), λ and μ are the 1st and 2nd Lamé parameters respectively, u is the displacement field, and t represents the time.

To solve the equation of motion for harmonic boundary condition, in general the plane wave solution is:

$$\vec{u}(\vec{r}, t) = u_0 \exp \left(i\omega \left(t - \frac{\vec{n} * \vec{r}}{c} \right) \right) \vec{e}_u \quad \text{with the position vector } \vec{r} = \begin{pmatrix} x_1 \\ x_2 \\ x_3 \end{pmatrix} \quad (3.15)$$

In (3.15) u_0 corresponds to the amplitude of the oscillation, \vec{n} is the wave normal vector, ω expresses the angular frequency (rad/s) and \vec{e}_u is the unit vector in the displacement direction.

The phase velocity is represented by c in (3.15) and it is directly proportional to its wavelength λ , such that, for a given frequency the faster is the waves the longer the wavelength:

$$c = \frac{\lambda\omega}{2\pi} \quad (3.16)$$

In the case of a compression wave the displacement oscillation is parallel to the direction of propagation \vec{n} and so by defining $\vec{e}_{\parallel\vec{n}}$ as the unit vector parallel to the direction of wave propagation, the (3.15) is written as:

$$\vec{u}(\vec{r}, t) = u_0 \exp\left(i\omega\left(t - \frac{\vec{n} * \vec{r}}{c_p}\right)\right) \vec{e}_{\parallel\vec{n}} \quad (3.17)$$

For a shear wave, the displacement oscillation is perpendicular to the direction of propagation \vec{n} , so naming $\vec{e}_{\perp\vec{n}}$ as the unit vector perpendicular to the direction of the propagation:

$$\vec{u}(\vec{r}, t) = u_0 \exp\left(i\omega\left(t - \frac{\vec{n} * \vec{r}}{c_s}\right)\right) \vec{e}_{\perp\vec{n}} \quad (3.18)$$

Furthermore can be defined the phase speed for each type of wave [22]. In particular, for a longitudinal wave the phase speed corresponds to:

$$c_p = \sqrt{\frac{\lambda + 2\mu}{\rho}} \quad (3.19)$$

For a transverse wave, the phase speed expression is:

$$c_s = \sqrt{\frac{\mu}{\rho}} \quad (3.20)$$

Lastly, (3.19) and (3.20) show how the two types of wave differ from each other. Indeed, as already mentioned, compression waves are characterized by a much longer wavelength than shear waves, therefore they are faster.

The two Lamé parameters are difficult to assess simultaneously since $\lambda \gg \mu$. For this reason, it is possible to partially filter out, with the use of a high filter, the influence of longitudinal wave because its spatial frequency is close to zero and it doesn't carry useful information to assess the mechanical property of tissue. Another solution is to apply a curl-operator, which is used to filter the contributions of the compression wave.

3.3 Torsional and Longitudinal case

It is fundamental to determine the effects of waves in a circular cylindrical rod, which represents the interested phantom, in both axial and torsional case. From [18] is possible to obtain the displacements and stresses as potential functions Φ and H , that satisfy the scalar and vector wave equations.

Cylindrical coordinates are used in this case and the scalar components for u are:

$$u_r = \frac{\partial \Phi}{\partial r} + \frac{1}{r} \frac{\partial H_z}{\partial \theta} - \frac{\partial H_\theta}{\partial z} \quad (3.21)$$

$$u_\theta = \frac{1}{r} \frac{\partial \Phi}{\partial \theta} + \frac{\partial H_r}{\partial z} - \frac{\partial H_z}{\partial r} \quad (3.22)$$

$$u_z = \frac{\partial \Phi}{\partial z} + \frac{1}{r} \frac{\partial r H_\theta}{\partial r} - \frac{1}{r} \frac{\partial H_r}{\partial \theta} \quad (3.23)$$

Consider τ as the stress, the boundary conditions for this problem are given by:

$$\tau_{rr} = \tau_{r\theta} = \tau_{rz} = 0, r = a \quad (3.24)$$

Using these conditions and note that harmonic waves may propagate in a cylinder, the resulting displacements and stresses are gained.

In particular, for torsional modes only u_θ displacement exists. And this displacement field is gained only if $H_z \neq 0$, resulting in:

$$u_\theta[x, r, t] = \begin{cases} Bre^{i(\xi x - \omega t)}, & \text{if } \beta = 0 \\ BJ_1(\beta r)e^{i(\xi x - \omega t)} & \text{if } \beta > 0 \end{cases} \quad (3.25)$$

Where B represents the amplitude and

$$\beta^2 + \xi^2 = k_f^2 = \frac{\omega^2 \rho}{\mu_\perp(1 + \phi) + T} \quad (3.26)$$

The boundary condition for the torsional case is $\tau_{r\theta} = 0$, the frequency equation for torsional waves is:

$$\beta a J_0[\beta a] = 2J_1[\beta a] \quad (3.27)$$

In (3.7) a corresponds to the radius of the considered cylinder. In the general case then, the steady state wave motion is

$$u_\theta[x, r, t] = B_0 r e^{i(\xi x - \omega t)} + \sum_{n=1}^{\infty} B_n J_1[\beta_n r] e^{i(\xi_n x - \omega t)} \quad (3.28)$$

For longitudinal modes $u_\theta = 0$ and the boundary conditions are

$$\tau_{rr} = \tau_{rz} = 0, r = a \quad (3.29)$$

and the displacements for this mode are represented by

$$u_r[x, r, t] = (-A J_1[r] + B i \xi J_1[\beta r]) e^{i(\xi x - \omega t)} \quad (3.30)$$

$$u_x[x, r, t] = (A i \xi J_0[r] - B \beta J_0[\beta r]) e^{i(\xi x - \omega t)} \quad (3.31)$$

Where A and B represents both amplitude and the ration is equal to:

$$\frac{A}{B} = - \left(\frac{\beta}{\alpha} \right)^2 \frac{\beta^2 - \xi^2}{2\xi^2} \frac{J_1[\beta a]}{J_1[\alpha a]} \quad (3.32)$$

Moreover

$$\alpha^2 + \xi^2 = k_p^2 = \frac{\omega^2 \rho}{k} \quad (3.33)$$

Where k is the bulk modulus of biological tissue and is 4 to 6 order of magnitude greater than μ_{\perp} and is reasonable to take $\alpha \ll 1$ and $\alpha \ll \beta$.

In this case $J_0[\alpha r] \simeq 1$ and $J_1[\alpha r] \simeq \alpha r/2$ and equation (3.30) and (3.31) can be simplified to the following

$$u_r[x, r, t] = (-A\alpha^2 r/2 + Bi\xi J_1[\beta r])e^{i(\xi x - \omega t)} \quad (3.34)$$

$$u_x[x, r, t] = (Ai\xi - B\beta J_0[\beta r])e^{i(\xi x - \omega t)} \quad (3.35)$$

3.4 Scalar Helmholtz Equation

MRE is used to evaluate viscoelastic shear properties of biological tissues by applying mechanical vibrations to them and detect then the response of the tissue through MRI.

Data processing in this case is characterized always by an inverse problem, obtaining information about the spatial distribution of elastic parameters from the displacement field [23]. There

are different methods to reach this objective, and they differ from noise, boundary conditions and also the property parameters of the tissue, such as viscosity, anisotropy and heterogeneity [24].

There are two types of approaches: the direct problem and the inverse problem. The direct problem can estimate the behaviour of a medium if the parameters μ , λ and the boundary conditions of the surface of the system are known [23]. Inversion techniques are iterative reconstructions or a direct inversion. In iterative reconstruction is determined the solution of the inverse problem and then the result is transformed in a repeated calculation of the corresponding direct problem. In this case, is used a finite-element model to assess the displacement field u_{calc} , such that it can be measured the difference between u_{calc} and u_{meas} , corresponding to the measured displacement field. Subsequently, there is an update of the parameter estimate, which is the input of FEM and is given by considering the information about boundary conditions and mechanical vibration path. The operation ends when the difference between u_{calc} and u_{meas} is lower than a predetermined threshold [23].

The main limits of this method are the high computational and the high dependency on boundary conditions that are not derived through experiments. The most used inverse method is the scalar Helmholtz equation that determines shear modulus which is related with the phase velocity of the wave equation.

In MRE the inverse problem can be solved by taking into account the tissues as a linear-elastic isotropic body, characterized by local homogeneity, such that boundary conditions and

stress field are neglected. The wave equation (3.14) needs the knowledge of 3D displacement because the equation for the individual components is coupled [25].

Transforming (3.14) into the frequency domain through the Discrete Fourier Transform and by assessing the elastic-viscoelastic analogy, which affirms that if the elastic solution of the wave equation is available, then the viscoelastic solution can be obtained in the frequency domain by replacing the elastic moduli with the corresponding complex (viscoelastic) moduli:

$$-\rho\omega^2\vec{U}(\omega) = (G_L(\omega) + G_S(\omega))\nabla(\nabla \cdot \vec{U}(\omega)) + G_S(\omega)\Delta\vec{U}(\omega) \quad (3.36)$$

In which $G_L(\omega)$ and $G_S(\omega)$ are the complex moduli representing the 1st and 2nd Lamé parameters respectively, ω the angular mechanical frequency and $\vec{U}(\omega)$ is the Discrete Fourier Transformation of the displacement [8].

Assuming incompressibility ($\nabla \cdot \vec{U}(\omega) = 0$), (3.21) becomes:

$$-\rho\omega^2\vec{U}(\omega) = G_S(\omega)\Delta\vec{U}(\omega) \quad (3.37)$$

This relation must hold for every direction in 3D space. Then, (3.22) is rearranged and the shear modulus is obtained:

$$G_S(\omega) = \frac{-\rho\omega^2\vec{U}(\omega)}{\Delta\vec{U}(\omega)} \quad (3.38)$$

The latter relation represents the scalar Helmholtz inversion. It is used by assuming the out of phase plane displacement into two-dimensional elastography and it returns an exact solution to the inverse problem considering the isotropy of the medium and local homogeneity.

In the 3D case to eliminate the contribution of the compression wave is used the curl operator in both sides of the equation (3.22). Since when the curl operator is applied to a gradient field the result is zero. So (3.22) becomes:

$$-\rho\omega^2\vec{Q} = G_S(\omega)\Delta\vec{Q} \quad (3.39)$$

In this case $\vec{Q} = \nabla \times \vec{U}$ represents a vector in each point in space (x,y,z) and only one parameter is unknown, which is the complex shear modulus. Hence, (3.24) illustrates an overdetermined problem and the exact solution do not exist. From linear algebra [26] it can be obtained the least-square solution, which is given by rewriting the complex shear modulus and substituting it in (3.24):

$$G_S(\omega) = -\rho\omega^2[(\Delta\vec{Q})^T(\delta\vec{Q})]^{-1}((\delta\vec{Q})^T\vec{Q} = \Delta((\nabla \times \vec{U})) \quad (3.40)$$

This relation does not equalize all three equations, but the error between the right and left side of (3.24) is minimized.

3.4.1 Multiparameter Inversion

In more realistic models the scalar Helmholtz inversion can not be used; since models are dependent on two or more parameters. In this case, another inversion technique is exploited and it is called AIDE (Algebraic inversion of the differential equation). Starting from MRE scan, this method is able to obtain different model parameters with independent parameters assuming local homogeneity [27],[28]. For example, considering a two-parameters Naiver equation:

$$\rho \ddot{\mathbf{u}} = (\lambda + \mu) \nabla(\nabla \cdot \mathbf{u}) + \mu \Delta \mathbf{u} \quad (3.41)$$

Considering now, the latter equation in the frequency domain. Through the derivative property of the Fourier Transform and by rearranging the right-hand side, equation (3.26) is written as:

$$-\rho \omega^2 \tilde{\mathbf{u}} = \lambda \cdot \nabla(\nabla \cdot \tilde{\mathbf{u}} + \mu \cdot (\nabla(\nabla \cdot \tilde{\mathbf{u}}) + \Delta \tilde{\mathbf{u}}) \quad (3.42)$$

Indicating the right hand-side in vector notation:

$$-\rho\omega^2\tilde{\mathbf{u}} = \mathbf{A} \cdot \begin{pmatrix} \lambda \\ \mu \end{pmatrix} \quad (3.43)$$

In which \mathbf{A} is a 3x2 matrix, characterized by 2^{nd} -order equation derivatives of the displacement field:

$$\mathbf{A} = [\nabla(\nabla \cdot \tilde{\mathbf{u}}), \nabla(\nabla \cdot \tilde{\mathbf{u}}) + \Delta\tilde{\mathbf{u}}] = \begin{pmatrix} \frac{\partial}{\partial x} \nabla \cdot \tilde{\mathbf{u}}, & \frac{\partial}{\partial x} \nabla \cdot \tilde{\mathbf{u}} + \Delta\tilde{u}_1 \\ \frac{\partial}{\partial y} \nabla \cdot \tilde{\mathbf{u}}, & \frac{\partial}{\partial y} \nabla \cdot \tilde{\mathbf{u}} + \Delta\tilde{u}_2 \\ \frac{\partial}{\partial z} \nabla \cdot \tilde{\mathbf{u}}, & \frac{\partial}{\partial z} \nabla \cdot \tilde{\mathbf{u}} + \Delta\tilde{u}_3 \end{pmatrix} \quad (3.44)$$

The elastic parameter it is solved using (3.28) such that [27]:

$$\begin{pmatrix} \lambda \\ \mu \end{pmatrix} = -\rho\omega^2 \cdot (\mathbf{A}^T \mathbf{A})^{-1} \mathbf{A}^T \cdot \mathbf{u} \quad (3.45)$$

Finally, this procedure consider also the displacement caused by the longitudinal wave in the system, since the 1st Lamé parameter is present.

3.5 Discretization and Noise

Once discrete data are measured, there is a chance to encounter discretization and noise, which lead to possible errors. Different measurements parameters can cause noise, including vibration amplitude and frequency, MR sequence sensitivity and other components related to MR sequence.

Furthermore, in the post-processing steps, in which is applied the inversion algorithm, is required the calculation of spatial derivatives. This process influences noise, amplifying it, because they act as a high-pass filter [27].

This behaviour is more present if the displacement has a low signal to noise ratio (SNR) and to overcome this problem must be applied a spatial filter that filter out the noise.

As mentioned, discretization leads to error in the displacement field. Indeed, considering a snapshot of a mechanical wave over space along a profile x , the length of a pixel spacing δx can affect the error and the calculation of spatial derivatives is falsified.

Discretization leads to an overestimation of wavelength. For instance, when two-dimensional mechanical wave is projected on a one-dimensional plane, the wave fronts of equal phase that passes through the plane, gives an overestimation of the measured wavelength. This is the main problem in wave theory, in which a lower dimensionality conduct to the danger in overestimating the wave length, unless the lower dimensionality is parallel to the direction of wave propagation [29].

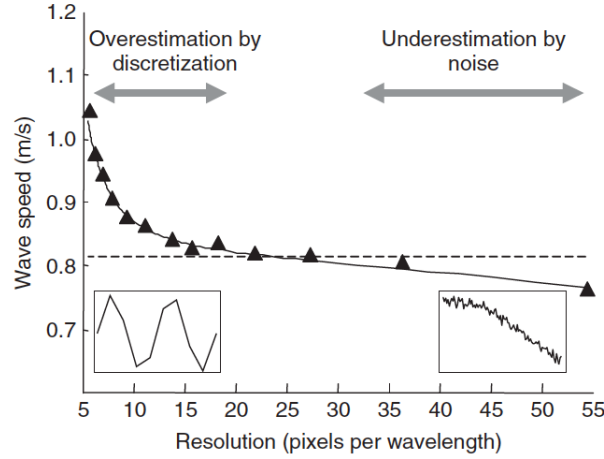


Figure 7: Illustration of the consequences of noise and discretization. The graph shows the wave speed (m/S) in relation to the resolution (pixel per wavelength). In the case of low resolution there is an overestimation by discretization and for higher resolution there is an underestimation given by noise

Finally, is observed from Figure 7 that for low resolution are dominant errors caused by discretization and elastic modulus is overestimated; on the other hand in case of high resolutions, noise occur effecting an underestimation of wave speed and elastic modulus [30].

3.5.1 Equation of motion for skeletal muscle

MRE investigates skeletal muscle, which is considered as one of the most plastic tissue present in human body[31]. Skeletal muscle possesses different functions. For instance, it converts chemical energy into mechanical energy to generate force, sustain posture and to create movements that affect daily-life activities. Additionally, skeletal muscle has a role in basal

energy metabolism, being storage for substrates, like carbohydrates, generating heat for the maintenance of temperature and oxygen consumption during physical activity [31].

Another important function is to be a reservoir of amino acids, which are used by other tissues for the synthesis of organ-specific proteins [32].

Skeletal muscle is constituted by a particular arrangement of muscle fibers and the respective connective tissue [31]. Muscle fibers are multi nucleated and each nucleus controls the type of protein synthesized in a nuclear domain which is a particular region of the cell. Between the sarcolemma and the basal lamina there are adult stem cells. They can proliferate and differentiate into new muscle fibers [33] have the function of muscle growing, repair and regeneration [31].

As it is indicated in Figure 8 an individual skeletal muscle is composed by hundreds or even thousands of muscle fibers bundled together in a connective tissue covering [34]. There are four main connective tissues that form the muscle. The Epimysium that surrounds each muscle, the fascia outside the Epimysium which separates the muscles. Then, inside the Epimysium the muscle is separated into compartments, and each of them contains a bundle of muscle fibers [34]. The Perimysium is the connective tissue that covers each bundle of muscle fiber and finally every muscle fiber is surrounded by the Endomysium.

A single muscle fiber has a length around 1 cm and a diameter of $100\ \mu\text{m}$ and each muscle fiber is surrounded by a cell membrane called Sarcolemma [31].

There are present different models that replicate skeletal muscle behaviour and their validity mainly depends on the material properties used to obtain model parameters. The architecture

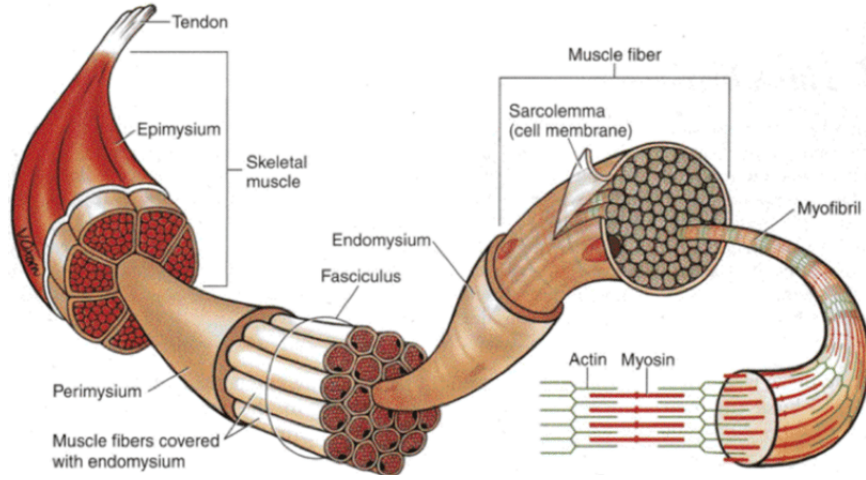


Figure 8: The figure illustrates the basic components of a skeletal muscle. Starting from the external layer, there is: the Epimysium, Perimysium that surrounds the muscle fibers and the Endomysium that covers each muscle fibers. Inside the Endomysium there is the Sarcolemma, which is the cell membrane. Finally inside the Sarcolemma there are Myofibrills that are constituted by two main proteins: Actin and Mysosin.

of skeletal muscle characterized by the parallel bundling of muscle fibers arranged serially, makes consider that the muscle can be transversely isotropic material, with the plane of symmetry defined by the longitudinal fiber axis [35].

Since MRE is capable of measuring different parameters of the tissue vibration anisotropy can be defined, through two-dimensional wave images. Furthermore the anisotropic material properties are obtained from wave patterns if the wave propagation is not restricted by the geometry of the excitation source and also if boundary conditions are non-reflecting [36].

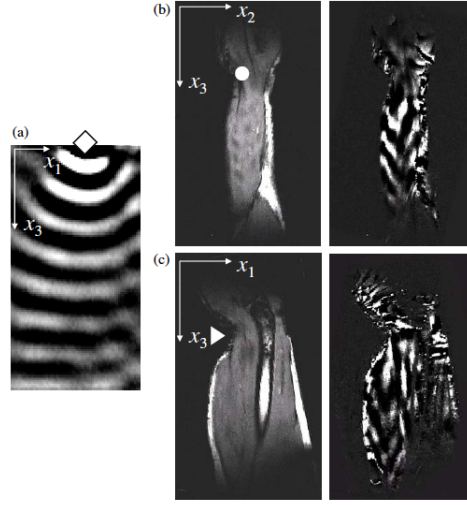


Figure 9: In figure (a) is represented the experimental shear waves in the case of agarose. On the left-hand side of (b) and (c) are illustrated the magnitudes of MRE representations. On the right-hand side of (b) and (c) are showed the experimental shear waves in a skeletal muscle of a right arm of the same subject, in sagittal and coronal slice position, respectively.

The waveform obtained in MRE acquisition is different depending on the elastic properties of the material analyzed. Precisely, from Figure 9 it is observed that in agarose for example the waveform is circular concentric and for a skeletal muscle is a V-shaped waves [36].

Consider now a Cartesian axes (x_1, x_2, x_3) the transverse isotropic model is showed in Figure 10 and it is described by positioning the principal axis of symmetry x_3 parallel to fibers of the muscle [36].

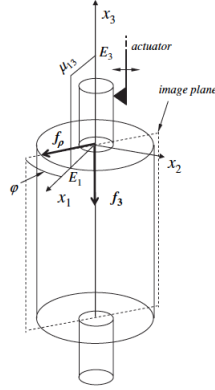


Figure 10: Representation of the tendon with actuator at the distal tendon. The image plane coincides with the stress plane, obtaining a planar stress situation. $\mathbf{f} = [f_\rho, f_3]$ is the resulting force vector and

The stress-shear relation for transverse isotropic linear elastic material is reduced to five independent material components.

$$\begin{pmatrix} \sigma_{xx} \\ \sigma_{yy} \\ \sigma_{zz} \\ \sigma_{yz} \\ \sigma_{xz} \\ \sigma_{xy} \end{pmatrix} = \begin{pmatrix} 2\mu_\perp + \lambda_\perp & \lambda_\perp & \lambda_M & 0 & 0 & 0 \\ \lambda_\perp & 2\mu_\perp + \lambda_\perp & \lambda_M & 0 & 0 & 0 \\ \lambda_M & \lambda_M & 2\mu_\parallel + \lambda_\parallel & 0 & 0 & 0 \\ 0 & 0 & 0 & \mu_\parallel & 0 & 0 \\ 0 & 0 & 0 & 0 & \mu_\parallel & 0 \\ 0 & 0 & 0 & 0 & 0 & \mu_\perp \end{pmatrix} \begin{pmatrix} u_{xx} \\ u_{yy} \\ u_{zz} \\ 2u_{yz} \\ 2u_{xz} \\ 2u_{xy} \end{pmatrix} \quad (3.46)$$

with σ_{ik} the stress tensor and u_{ik} being the strain tensor. These five material parameters are μ_{\perp} and μ_{\parallel} , that symbolize the two shear moduli, representing the shear wave that propagates in the parallel and perpendicular direction of the fiber [37]. The other three parameters λ_M , λ_{\parallel} and λ_{\perp} describe different directions of propagation of the longitudinal wave. The (3.31) can be written also exploiting the displacement vector \mathbf{u} :

$$\rho \partial_t^2 u_i = \frac{\partial \sigma_{ik}}{\partial x_k} + \zeta \partial_t \nabla^2 u_i + (\xi + \zeta) \frac{\partial^3 u_k}{\partial_t \partial x_i \partial x_k} \quad (3.47)$$

In which ζ figures the shear viscosity and ξ is the viscosity of the longitudinal wave, which is neglected at lower frequencies. Also, ζ , ξ and $\nabla \mathbf{u}$ are small quantities, such that the third part on the right-hand side of the equation is neglected as well. Inserting (3.31) in (3.32) the equation of motion is:

$$\rho \partial_t^2 \mathbf{u} = \mu_{\perp} \nabla^2 \mathbf{u} + (\lambda + \mu_{\perp}) \nabla (\nabla \mathbf{u}) + \tau \begin{pmatrix} \frac{\partial^2 u_x}{\partial z^2} + \frac{\partial^2 u_z}{\partial x \partial z} \\ \frac{\partial^2 u_y}{\partial z^2} + \frac{\partial^2 u_z}{\partial y \partial z} \\ \nabla^2 u_z + \partial_z (\nabla \mathbf{u}) \end{pmatrix} + \zeta \partial_t \nabla^2 \mathbf{u} \quad (3.48)$$

In the latter equation $\tau = \mu_{\parallel} + \mu_{\perp}$ and assuming an incompressible medium it can be stated that $\lambda = \lambda_{\parallel} = \lambda_{\perp} = \lambda_M$. Moreover, in case of isotropy $\tau = 0$ and (3.33) is valid for both

components u_r (the divergence-free part of the displacement field) and u_L (curl-free part of displacement field) [37].

τ is in the order of the shear modulus and assuming a steady state (3.33) can be expressed using PDE considering only the transverse contribution:

$$-\rho\omega^2\mathbf{u}_T \simeq \mu_\perp \nabla^2 \mathbf{u}_T + \tau \begin{pmatrix} \frac{\partial^2 u_x^T}{\partial z^2} + \frac{\partial^2 u_z^T}{\partial x \partial z} \\ \frac{\partial^2 u_y^T}{\partial z^2} + \frac{\partial^2 u_z^T}{\partial y \partial z} \\ \nabla^2 u_z^T \end{pmatrix} + \zeta\omega \nabla^2 \vec{\mathbf{u}}_T \quad (3.49)$$

$\vec{\mathbf{u}}_T$ represents the displacement vector shifted by $t = \pi/2\omega$ in time. Ultimately, to solve (3.34) is needed the knowledge of \mathbf{u}_T and it is valid when axis of the fiber and the z-axis of the coordinate system are coincident. Further insights are explored and analyzed in [37].

In general, for a incompressible, transversely isotropic material there are three independent parameters by combining two tensile and shear moduli, E_\perp , E_\parallel , μ_\perp and μ_\parallel respectively [38]. In particular, E_\perp and μ_\perp are perpendicular to the direction of the fibers and so parallel to the plane of isotropy, on the other side E_\parallel and μ_\parallel are parallel to the fibers. Take into consideration a shear wave propagating in an arbitrary direction equivalent to an angle θ from the direction of the fibers and through a material incompressible transversely and isotropic. The displacement of the shear wave is polarized in two different independent components: a shear

and a fast wave. The slow shear wave presents the direction of polarization perpendicular to the direction of the fiber and also of the propagation. Therefore, the polarization is in the z direction, considering the fibers in the y direction and propagation in the x-y plane [38].

The speed of the shear is:

$$c_s^2 = \frac{\mu_{\perp}}{\rho}(1 + \phi \cos^2[\theta]) \quad (3.50)$$

In which Φ represents the shear anisotropy and is equal to $\phi = \mu_{\parallel}/\mu_{\perp} - 1$.

The slow shear wavelength $\lambda_s = c_s/f$, in which f is the frequency in Hertz. The ratio between the slow shear wavelength that it is parallel to the fibers $\lambda_{s\parallel}$ and the one perpendicular to the fibers $\lambda_{s\perp}$ corresponds to $\lambda_{s\parallel}/\lambda_{s\perp} = \sqrt{1 + \phi}$. Regarding, the fast shear waves, characterized by a polarization direction that is not perpendicular to the fiber direction, have speed c_f given by:

$$c_f^2 = \frac{\mu_{\perp}}{\rho}(1 + \phi \cos^2[2\theta] + \zeta \sin^2[2\theta]) \quad (3.51)$$

Where ζ corresponds to the tensile anisotropy, and corresponds to $\zeta = E_{\parallel}/E_{\perp} - 1$. The fast shear wavelength λ_f corresponds to the ratio between the speed wave c_f and frequency f : $\lambda_f = c_f/f$.

Consider now, T as the amplitude of an uniaxial initial or pre-stress, parallel to the axis of

isotropy. By neglecting higher order and nonlinear effects due to the deformation caused by T , the speed of slow and fast shear waves can be expressed as:

$$c_s^2 = \frac{\mu_{\perp}}{\rho} \left(1 + \phi \cos^2[\theta] + \frac{T}{2\mu_{\perp}} \cos^2[\theta] \right) \quad (3.52)$$

$$c_f^2 = \frac{\mu_{\perp}}{\rho} \left(1 + \phi + \frac{T}{2\mu_{\perp}} \cos[2\theta] + (\zeta - \phi) \sin^2[2\theta] \right) \quad (3.53)$$

With these two latter equations a relationship between the pre-stress T and the intrinsic material viscoelastic properties μ_{\perp} , ϕ and ζ can be defined.

3.6 Viscoelastic models for biological tissue

In MRE experiments at multiple frequencies are exploited specific viscoelastic models, in order to obtain more accurate information about mechanical properties and to reproduce the viscoelastic behaviour of the muscle. These rheological models can be of two, three or four independent constitutive parameters [39][40]. Depending on the imaging data obtained each model affects tissue property estimation. More specifically, models with a lower number of free parameters are preferred [40], because they can recognize with more sensitivity and specificity viscoelastic changes. Thus, they can be a powerful tool for clinical perspective.

A harmonic plane wave (3.15) is written also as a function of the wave speed c and the wave

damping coefficient γ [40], such that they can be related to complex shear modulus G discussed in paragraph 3.3:

$$u = u_0 \exp \left[i\omega \left(\frac{\mathbf{n} \cdot \mathbf{r}}{c} - t \right) - \gamma \mathbf{n} \cdot \mathbf{r} \right] \quad (3.54)$$

Putting together (3.35) and (3.23) the wave speed and the wave damping are respectively equal to:

$$c(\omega) = \frac{1}{\Re \left[\sqrt{\frac{\rho}{G(\omega)}} \right]} \quad \text{and} \quad \gamma(\omega) = \omega \Im \left[\sqrt{\frac{\rho}{G(\omega)}} \right] \quad (3.55)$$

In which, \Re and \Im express the real and imaginary part of a complex number. Using now different rheological models the complex shear wave modulus is characterized by different values of elasticity and viscosity. The most used models are listed in Figure 11 with their respective complex shear modulus value.

The main elements that compose all these models are a spring, which represents the energy storage of the system, a dashpot that characterizes the damping part of the system, and then a springpot, which is an interpolation between a spring and a dashpot.

Voigt and Maxwell's models require just the knowledge of the shear modulus (μ) and shear viscosity (η) [39].

The Springpot model instead, intrinsically associates the dynamics of the complex shear modulus to the fractal geometry of components that build the mechanical scaffold of tissue. In particular, this model is characterized by two free parameters, k and α , which leads to predict

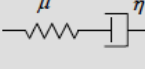
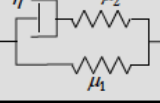

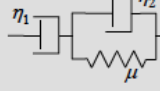

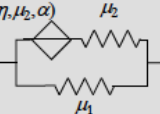
<p>Maxwell</p>  $G(\omega) = \frac{i\omega\eta\mu}{\mu + i\omega\eta}$	<p>Zener</p>  $G(\omega) = \mu_1 + \frac{i\omega\eta\mu_2}{\mu_2 + i\omega\eta}$
<p>Voigt</p>  $G(\omega) = \mu + i\omega\eta$	<p>Jeffreys</p>  $G(\omega) = -\omega\eta_1 \frac{\omega\eta_2 - i\mu}{\mu + i\omega(\eta_1 + \eta_2)}$
<p>Springpot</p>  <p>(η, μ, α) $(\eta: \text{constant}, 0 > \alpha > 1)$</p> $G(\omega) = \mu^{1-\alpha} (i\omega\eta)^\alpha$	<p>4-Parameter Zener</p>  $G(\omega) = \mu_1 + \frac{\mu_2 \left(\frac{i\omega\eta}{\mu_2} \right)^\alpha}{1 + \left(\frac{i\omega\eta}{\mu_2} \right)^\alpha}$

Figure 11: Illustration of the most used viscoelastic models with the respective value of the complex shear modulus: Maxwell, Voigt, Zener, Jeffreys and fractional Zener. Below that are represented the rheological elements from the spring, dashpot and springpot, a combination between the spring and dashpot.

the changes of two fractions over frequency ω .

In this case, the stress and deformation relation in the frequency domain corresponds to:

$$\sigma(\omega) = \mu_\alpha^{1-\alpha} (i\omega\eta)^\alpha \epsilon(\omega) \quad (3.56)$$

μ_α and α are assigned to principal patterns of structural changes, therefore these parameters have a physical meaning related to the structural properties of the model, highlighting a relationship between histology and Elastography parameters. The stiffness is represented by μ_α and it is the viscoelastic connectivity between the individual elements and the stiffer is the

tissue the higher is the value of μ_α . Differently, α is a weighting factor and describes the matrix geometry, meaning that is related to the geometrical reordering of the structure [16]. Its value is $0 \leq \alpha \leq 1$. Specifically, for $\alpha = 0$ the springpot becomes a spring and for $\alpha = 1$ it is reduced to a dashpot. Overall, the more parameters are used in a model the more components and aspects of soft tissues can be considered. On the other hand, more free parameters lead to more sensitive fitting process and it could bring noise. Thus, in an Elastography clinical study is important to find a right compromise between number of parameters, obtaining a stable and accurate system [40].

CHAPTER 4

STATE OF THE ART

4.1 Torsional Actuation experiments

A previous work has been done at the University of Illinois at Chicago, in which it was assessed the mechanical properties of a phantom through torsional vibration with a Table Top MRI System [41]. The torsional vibration was generated through the same Stepper Motor, provided by the German company Pure Devices. The set up was characterized by a black rod, which was connected to a rotating disk that created the torsional vibration of the sample. In the study, to reduce attenuation at higher frequencies, it was used a steel coupler composed of two sets of screws on its top and bottom end, such that the first pair was connected to the rotating shaft and the second pair is attached to a component made of *VeroClear*. The other half of this latter piece was wrapped around the plastic rod, used to hold the test tube. Inside the test tube, there was inserted a sample, which was placed at a certain height in the region of interest of the Table Top System. The set up was then constituted by the Stepper Motor attached to an acrylic support base, that is then leaned to the Table Top MRI System (Figure 12).

In this study, were analyzed different samples: an isotropic gelatin sample, an anisotropic sample containing carbon fibers in a soft plastic matrix, to simulate real muscle structure, and

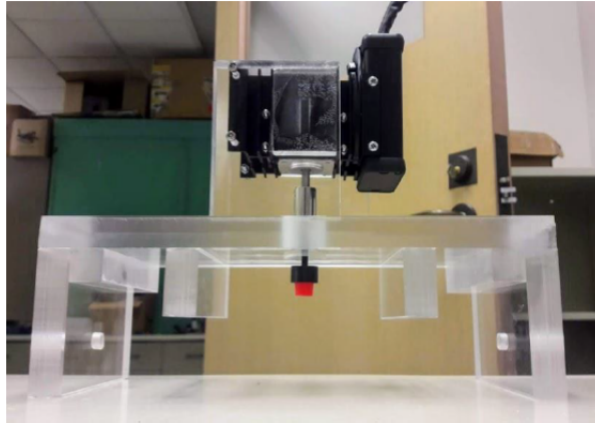


Figure 12: Setup composed by Stepper motor, with the black plastic rod, the Vera clear component that connect the coupler to the rod and the acrylic support base

also it was considered muscle samples extracted from a calf and a thigh of a mouse.

Results showed that were not present clear wave-fronts for both isotropic and anisotropic samples and this could be because of very little ROI. Furthermore, it was understood that to obtain a better number of wave-fronts, higher frequencies need to be applied to the system, considering also that as the frequencies increase the attenuation is more evident [41].

4.2 Table Top System

In general a Table Top MRI scanner is a tool that demonstrates different concepts like magnetic resonance, spatial encoding or Fourier transform [42]. Indeed in MRE is used in combination with a mechanical vibration in order to estimate elastograms.

There are different types of low-cost Table Top imaging systems. In this work is exploited Pure Device 0.5T Table Top system from Germany. The device is for both scientific and industrial applications. Moreover, the efficient and compact design give the opportunity to be used also in laboratory settings, since it gives the chance to examine different samples [43].

The all system is then characterized by different components [42],[44]. First, the magnet with a magnetic field of 0.5T, then the Gradient coils used for imaging. Indeed, they produce a magnetic field in the z direction that changes linearly with position. Other components are the Gradient Power Amplifier (GPA) which is needed to supply current to the gradient coils, and the RF subsystem to guarantee RF transmission and reception. Lastly, there is a Matlab software able to conduct experiments.

4.3 Phantom

Different materials can be taken into account when it come to create a sample. Particularly, in this work it has been used *Ecoflex*TM (SMOOTH-ON, INC., USA).

*Ecoflex*TM is a versatile platinum-catalyzed silicone and it is useful in MRE experiments since it is a material that tends to change less over time compared to water-based gelatin or agar gel. *Ecoflex*TM over time has good durability and reasonable stability [40]. Moreover, its deformation response is close to soft biological tissue. Indeed, the mechanical behaviour of *Ecoflex*TM tends to yield a linear strain limit near to soft biological tissue. For instance, the mechanical behaviour of *Ecoflex*TM tends to yield a linear strain limit near to 30% at a strain rate of 50 mm/min considering a dumbbell specimen with 30 mm in length when it is in tension [45].

Exist different types of hardness of *Ecoflex*TM (00-10, 00-20, 00-30 and 00-50) and the higher is the number that characterized the type of *Ecoflex*TM the stiffer is the phantom. Hence, by changing the material stiffness mechanical properties can be controlled.

CHAPTER 5

MATERIAL AND METHODS

5.1 Preparation of the isotropic phantom

The phantom used in this work is made of *Ecoflex*TM 00-30, a material soft enough to mimic the muscle and soft biological tissue. In order to obtain the sample, the first step was to stir Part A and Part B, then in a container was poured and mixed a 1A:1B by volume or weight mix ratio. After about three minutes of mixing, there was a vacuum degassing phase, to eliminate entrapped air.

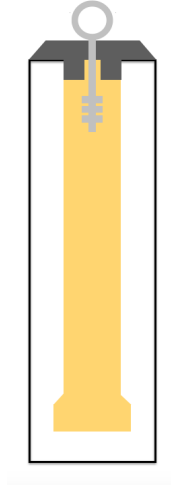


Figure 13: Diagram of the mold used to create the *Ecoflex*TM 00-30 phantom. The dark grey component is the Endcap, the grey part is the Anchor and in yellow is represented the Ecoflex phantom, which is placed inside the mold.

When this last phase was finished, the mixture was poured on a designed mold and it was cured for four hours at room temperature with negligible shrinkage. The phantom at the top features a flange, so that the phantom can be grabbed by an Adapter, that will be described further on. Moreover, while it cures at the bottom part was inserted a little Anchor, that also will be described in more details in the following section.

The phantom has a length of 120 mm a diameter of 8 mm with the flange has a 12 mm diameter. A diagram of the whole phantom setup is represented in Figure 13, characterized by the Anchor, the Endcap and the *Ecoflex*TM 00-30.

5.1.1 Anchor and Endcap

The Anchor showed in Figure 14 is 30 mm long, made of *Siraya Tech Fast* created with *PhotoT Mono SE 3D printer by Anycubic*. It was directly inserted into the phantom during its curing, so that there was no need of any additional component to bond them together. In addition, to make sure that the Anchor was fixed to the bottom part of the sample, it was applied a Silicone modified conformal coating by *MGchemicals*[®] to the Anchor.

The purpose is to hang through a fishing line (*KastKing Superpower Fishing Line, 6LB 327YDS*) different bullet weights, in order to analyze how shear waves propagates in a pre-strain sample.



Figure 14: 3D illustration of the weight anchor.

It is created an Endcap (Figure 15), made of the same material and with the same 3D machine of the mold and of the Anchor. The Endcap is an additional system to guarantee the attachment of the Anchor to the phantom.

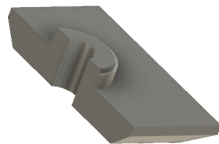


Figure 15: 3D illustration of the Mold Endcap .

5.1.2 Weights

The bullet weights (Figure 16) are made of lead, a non-magnetic material, thus it was possible to hang them to the anchor, through a fishing line, causing an elongation of the sample. The elongations observed in this study were of 10% and 20%, by using and combining together lead weights of 0.48oz, 0.68oz and 1.05oz.

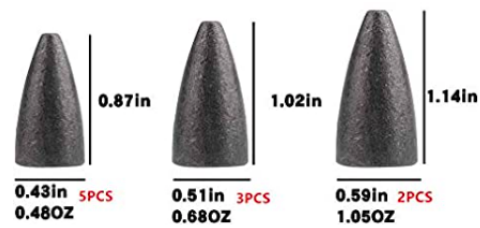


Figure 16: Lead bullet weights used in the setup.

5.2 Setup mechanics

The setup used it is characterized by the MRI Benchtop 0.587T system (*Pure Devices GmbH, Würzburg, Germany*) that comprise of:

1. The Control driver;
2. The 0.587T (25MHz) magnet (magspec);
3. The pre-amplifier;

4. The high-power gradient amplifier (DC-600);
5. The RJ-45 adapter connected to the actuator;
6. The actuator supports and sample holder.

The setup is characterized by a Matlab software that derives wave images. The Magnet case is not perfectly symmetric with respect to the bore and the reference of the system has the y axis aligned with the axis of the sample considered (Figure 17).

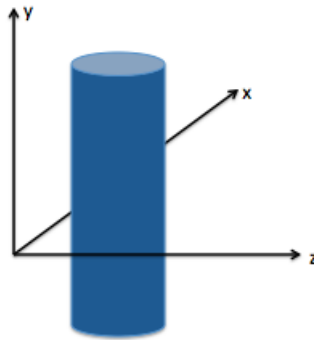


Figure 17: Reference system in the Table Top MRI Scanner.

5.2.1 Actuators

The actuators exploited to transmit motion to the phantom were a piezoelectric actuator *PAHL60/20* (Piezosystem jena) which creates an axial displacement and a Stepper Motor actuator *14HS13 – 0804S* (Stepperonline) for torsional vibration.

5.3 Preliminary testing

At the beginning of the study, the experiments were focused on the Stepper Motor. Accordingly to fix the phantom to the rest of the setup was designed another piece: the Adapter. Its length is 31mm and it is made of *Siraya*[®] Tech Fast and it is constituted by two equal and symmetric parts, such that when the phantom was ready, the two pieces were glued together Figure 18.



Figure 18: 3D illustration of the 3D stepper Motor adapter.

A steel coupler is utilized to bind the rod to the Stepper Motor, since it is constituted by two sets of screws on both top and bottom end. In particular, the top pairs were attached to the protruded rotating shaft of the actuator and the bottom part coupled the rod. The diameter of the elongated rod is 5 mm, length 21 mm and it is screwed with a M4 thread.

The Stepper Motor is placed then on the magnet through a pre-existing acrylic support base (267 mm x 115 mm x 92 mm), built utilizing clear scratch and UV resistant cast acrylic sheet made in the Acoustic and Vibrations Laboratory at UIC, showed in Figure 20.

This set up with the phantom at the rest position (meaning that no weight was hung to the system) has been implemented with the Table Top MRI scanner for a preliminary testing. It was used a frequency of 500Hz and from the wave images obtained it was showed that attenuation was strongly present.

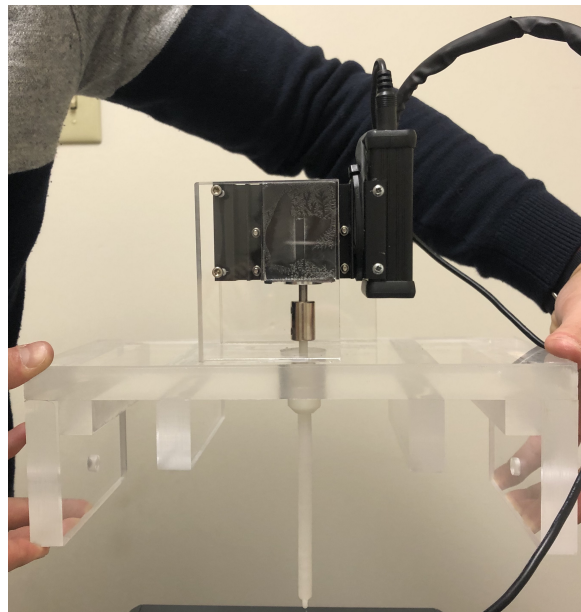


Figure 19: Representation of the Stepper Motor setup with the sample.

5.4 Stepper Motor and Piezoelectric setup

A possible solution to overcome the attenuation was to idealize an extension of 60 mm to the Adapter mentioned in Section 5.3, as showed in Figure 20.

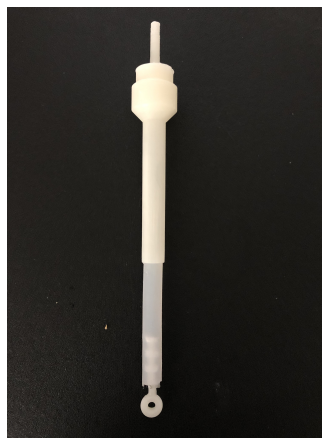


Figure 20: Illustration of the new design of the phantom, realized with the new adapter.

In this case, the new phantom has been tested by using both the Stepper Motor and the Piezo actuator. For this reason the rod of the new Adapter was made with a M4 thread, so that it could be screwed into the Piezoelectric actuator.

This modification has led to change also the Stepper Motor setup. Indeed, there was the introduction of a new part already available in the laboratory, a *VeroClear* piece, that allowed the connection of the new threaded hole to the steel coupler: one side of the component is

inserted inside the coupler and the other side is fixed to the new rod of the Adapter, that grabs the phantom. The two actuators are connected to a pre-existing acrylic structure made of clear scratch and UV resistant cast acrylic sheet with different dimensions. The one for the Stepper Motor has been already described in Section 5.3 and it is represented also in Figure 21. The other one, considered for the Piezo actuator, has a dimension of 267 mm x 60 mm x 85 mm and it is illustrated in Figure 22.

5.5 Setup with two piezoactuators

To compare and cross-validate the results obtained by the Stepper Motor, for a torsional vibration it has been idealized another setup. The support structure is the same one used from the previous Stepper Motor setup.

Two $P - 842.10$ (PI) piezoelectric actuators are combined together in a counter-phase configuration, generating a torsional vibration.

Particularly, $P - 842.10$ is sensitive to bend forces. A possible solution to avoid them is to screw onto the tips of the piezoactuators a corresponding 176.50 flexible tips (Figure 23).

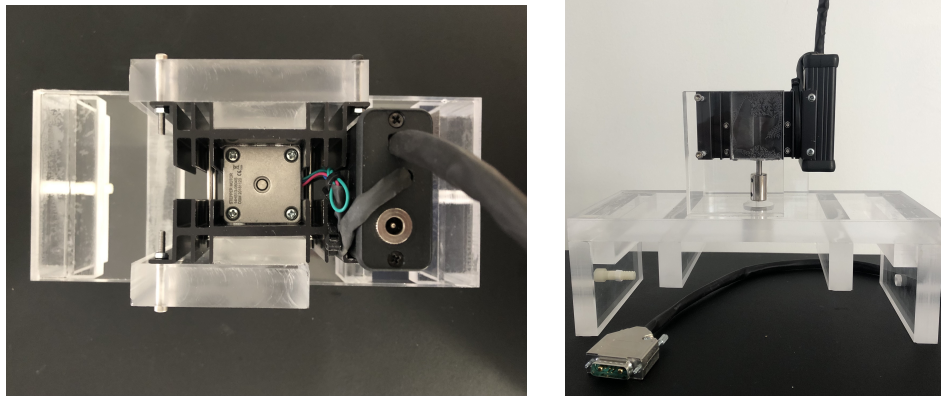


Figure 21: Stepper Motor actuator 14HS13 – 0804S with the respecting acrylic structure. On the left is showed the top view and on the right side the front view.

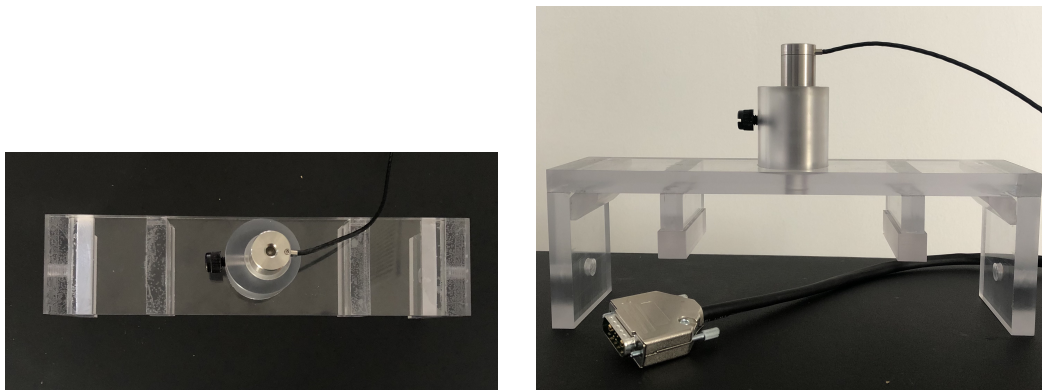


Figure 22: Piezoelectric actuator PAHL60/20 with the respecting acrylic structure. On the left is showed the top view and on the right side the front view.

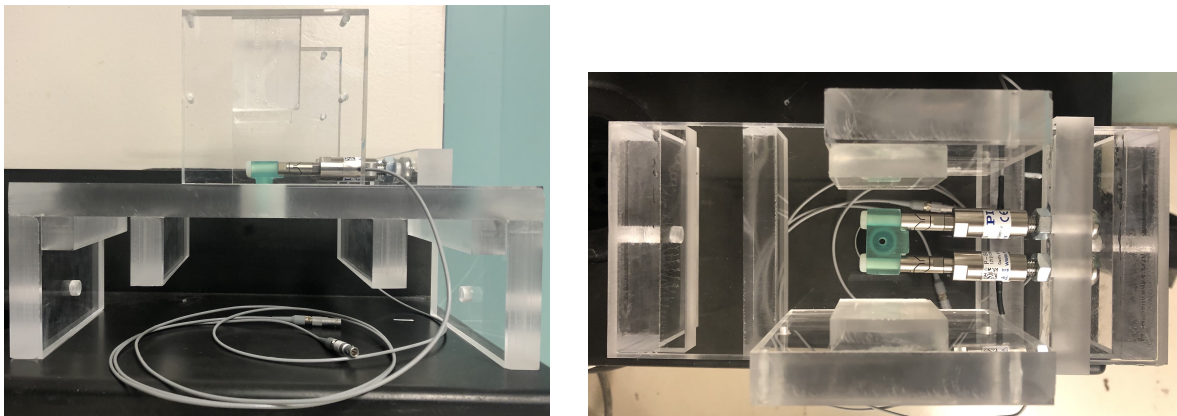


Figure 23: Top view and front view of the setup with two piezoactuators.

The main components of this new setup are:

1. Two M8 screws screwed on the two piezos to fix the system;
2. Two washers, previously present in the laboratory, screwed to the M8 screws with the purpose of protection of the material and antiloosening of the system;
3. A solid acrylic structure, glued on the support base, positioned between the two M8 screws and the two actuators, allowing for a more stabilized structure;
4. The two piezos $P - 842.10$ connected to the two 176.50 flexible tips;
5. The holder, a 3D printed component, 33mm long and a width of 20 mm (Figure 24). It is inserted in the support base and exhibits two holes to allow the junction of two M5 plastic screws with the two flexible tips, by using M5 screws. The holder is not fixed, and connects together the phantom to the rest of the system, such that when the two actuators are activated, the motion is transmitted to the phantom. Indeed at the bottom of the holder has a M4 screw hole screwed such that it is screwed the rod of the adapter.

Moreover, for this setup the rod attached to the phantom was made of a stronger resin, *Siraya*[®] Tech Blu, instead of *Siraya*[®] Tech Fast as it showed Figure 25. This choice was made in order to guarantee a more secure connection between the rod and the adapter glued to the phantom. Moreover the rod itself, it is M4 thread screwed, so it can inserted in the holder.

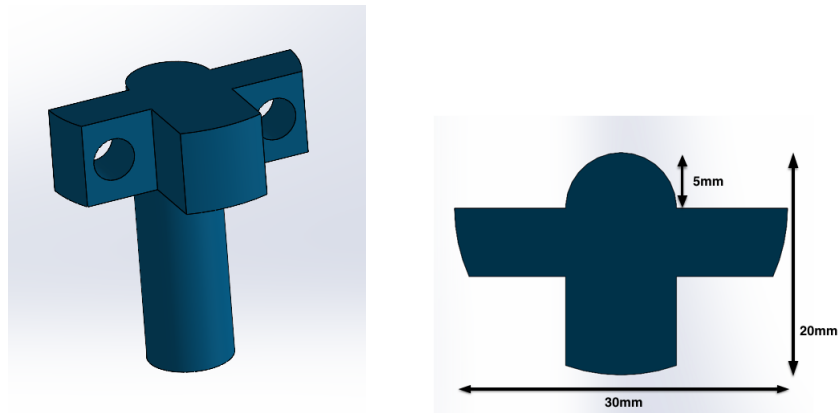


Figure 24: Representation in 3D of the holder component on the right. On the left it is illustrated the top view of it, with the respective measurements



Figure 25: Phantom with the new adapter.

5.6 MRE computational study

The results obtained from the experimental setup were compared with the results of computational study. The MRE finite elements simulations were done using *COMSOL Multiphysics*® 5.3a (Stockholm, Sweden).

The phantom used for the measurements was imported from SolidWorks, with a length of 120mm and a diameter of 8mm.

Once the geometry is defined, the next step is to implement the material properties that reflect the examined phantom in the experimental analysis.

The input parameters are the mechanical properties of the *Ecoflex*™ 00-30 and the complex shear modulus acquired considering the Fractional Voigt viscoelasticity model, described in [46] and mentioned in Chapter 3.5 (Table I).

Parameters (symbol)	Expression	Value
Radius (r)	0.004 <i>m</i>	0.004 <i>m</i>
Length (L)	120 <i>mm</i>	0.12 <i>m</i>
Density (ρ)	1000 <i>Kg/m</i> ³	1000 <i>Kg/m</i> ³
Frequency (f)	500 <i>Hz</i>	500 <i>Hz</i>
Young's modulus (E)	5.4214·10 ⁵ <i>Pa</i>	5.4214·10 ⁵ <i>Pa</i>
First Fractional Voigt model (μ_α)	1.956 <i>Pa</i>	1.956 <i>Pa</i>
Second Fractional Voigt model (α)	0.34	0.34
Poisson's ratio (ν)	0.4999913	0.4999913
Tensile strength (μ_0)	1.379·10 ⁶ <i>Pa</i>	1.379·10 ⁶ <i>Pa</i>
Real shear modulus (μ_{Re})	$\mu_0 + \mu_\alpha \cdot 2\pi f \cos(\alpha\pi/2)$	1384289.22 <i>Pa</i>
Imaginary shear modulus (μ_{Im})	$\mu_\alpha \cdot 2\pi f \sin(\alpha\pi/2)$	3128036.7 <i>Pa</i>
Complex shear modulus (μ)	$\mu_{Re} + \mu_{Im}$	1384289.22 + <i>i</i> 3128036.7 <i>Pa</i>
Bulk modulus (k)	$\frac{E(1-\nu)}{(1+\nu)(1-2\nu)}$	5.99·10 ⁶ <i>Pa</i>
Displacement (k)	11.6·10 ⁻⁶ <i>m</i>	11.6·10 ⁻⁶ <i>m</i>

TABLE I: Input parameters in COMSOL

For all simulations it was exploited a *Finer* mesh, and as for the experimental setup, were considered strain of 0%, 10% and 20% with respect of the length of the phantom when it is at rest.

Moreover were considered both, axial and torsional excitation. Therefore for the axial vibration, it was applied to the entire lateral surface of the geometry a uniform boundary condition of $11.6 \mu m$ harmonic shear displacement in the y direction. On the other hand, for the torsional displacement, the displacement was still $11.6 \mu m$ but applied in the x and z direction.

Finally, the frequencies investigated are the same used for the experimental setup, thus 200Hz, 400Hz, 600Hz, 800Hz and 1000Hz.

CHAPTER 6

RESULTS AND DISCUSSION

6.1 Examination of motion

Once the setup is ready, it is important to examine if there is actual motion transmitted to the sample during the analysis. For this reason, to examine the Stepper and the Piezoelectric setups, it has been used a more sensitive system than the MRE itself, which is the *Polytec PDV – 100* Portable Digital Vibrometer (Figure 26). It is a portable digital laser vibrometer and it gives accurate and precise measurements of the vibration velocities in a frequency range that reaches 22 kHz. One of the main advantage was also that it can be used without being in contact with the sample [47].



Figure 26: Representation of the *Polytec PDV – 100* Portable Digital Vibrometer.

In general, a Laser Doppler Vibrometer (LDV) is a tool capable of making vibration evaluations being non-in-contact with the surface considered. The working principle of the LDV is based on the Doppler effect, which allows to acquire the vibration velocities.

The laser beam projected by the LDV is aimed at the sample's surface and this causes a shift of the Doppler frequency of the reflected laser beam because of the vibration of the sample itself. In the end, the result is a voltage value directly proportional to the velocities of the target over the laser beam's direction [48].

A reflective tape was attached to the sample, so that the light beams are reflected and measurements can be done, in order to analyze vibration.

The LDV is connected then to a dynamic signal analyzer *Agilent 35670A* that evaluates mechanical vibration applied on the phantom and characterizes control systems or network analysis. Indeed, for this study in the display were illustrated two graphs: one in time domain that shows the wave form of the signal, comparing sinusoidal versus distorted signal; and the other one in frequency domain, to validate that the system is working at the expected frequency.

6.1.1 Axial excitation

First it was evaluated the piezoelectric setup. Once the phantom was connected to the system and the whole setup was placed outside the magnet, the laser beam of the LDV was focused towards the reflective tape attached to the phantom.

In order to confirm motion of the phantom, experiments at different frequency were considered. Figure 27 represents an example of what was obtained after running the setup at 200 Hz. In

the top graph is represented the peak amplitudes values (pk) over time (s), in the second one at the bottom, there is the root-mean-square value (rms) over frequency (Hz).

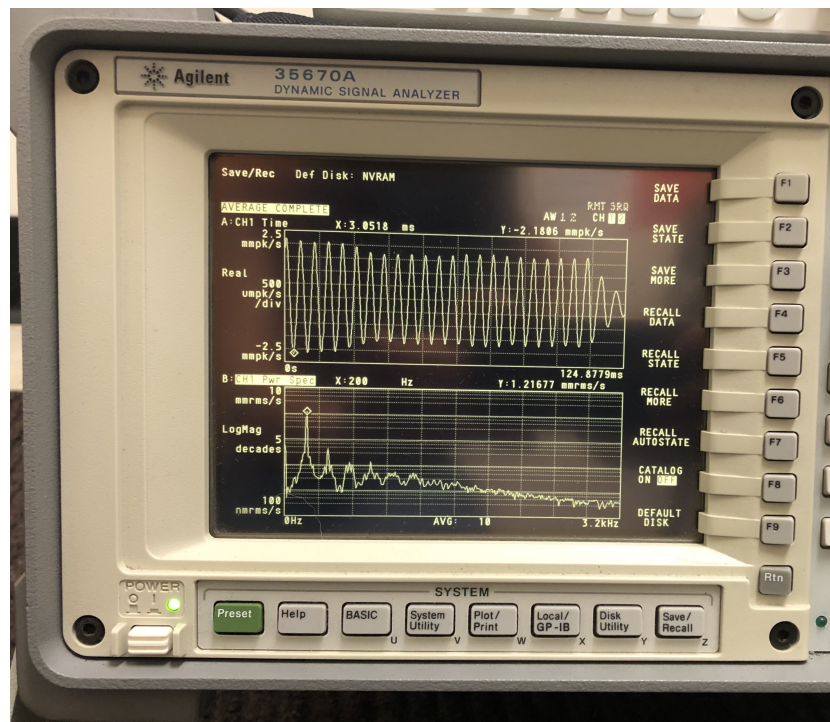


Figure 27: Representation of displacement and frequency values using *Agilent 35670A*.

The LDV was done also taking into account other frequencies and the respective displacement was measured. The values are illustrated in Table II below:

Frequency [Hz]	Amplitude [mm/s]	Displacement [mm]
200	2.1806	0.00174
300	0.1556	0.00008
400	2.1449	0.00085
500	4.7794	0.00150

TABLE II: Displacement measured from the results obtained by the *Agilent 35670A* for 200, 300, 400, 500 Hz using the Piezoelectric.

Using both graphs it was possible to demonstrate that there was enough motion transmitted to the phantom, since the values obtained were of the order of micrometers, and that frequencies corresponded to the one expected from each experiment.

6.1.2 Torsional excitation

The same application and measurements were done for the torsional vibration using the Stepper Motor setup. The results are represented in Table III.

From the table it was clear to notice that the displacement values are much lower than the axial vibration, but still good enough to use the setup for MRE experiments.

Frequency [Hz]	Amplitude [$\mu\text{m/s}$]	Displacement [μm]
200	20.15	0.0160
300	123.92	0.0657
400	215.73	0.0687
500	16.42	0.0052

TABLE III: Displacement measured from the results obtained by the *Agilent 35670A* for 200, 300, 400, 500 Hz using the Stepper Motor.

6.2 MRE experiments

6.2.1 Piezoelectric actuator

The piezoelectric setup was not used for further experiments since, with the new phantom setup, axial excitation will mainly drive quasi-longitudinal waves along the axis of the phantom. These considerations can be showed in Figure 28, in which experiments have been done through the Table Top by using a frequency of 200 Hz. It is represented the real and imaginary part of the complex displacement of the wave images with the different frequencies along the columns. The second figure illustrates the absolute and the phase of the complex wave images with the different frequencies along the columns.

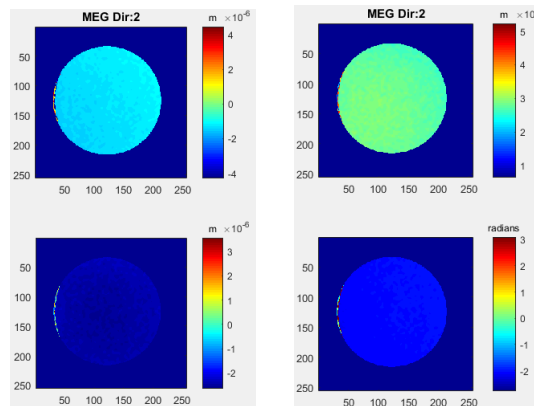


Figure 28: On the left is showed the real (top) and imaginary (bottom) part; on the right the absolute (top) and the phase (bottom) values of the complex wave image for 200Hz.

6.2.2 Stepper Motor actuator

Experiments were done then with the Stepper Motor setup and shear waves were analyzed at 200Hz, 400Hz, 600Hz and 800Hz and 1000Hz. The results are showed in Figure 29, Figure 30, Figure 31, Figure 32 and Figure 33 in which the real-imaginary part and absolute-phase part are represented in x and z direction respectively.

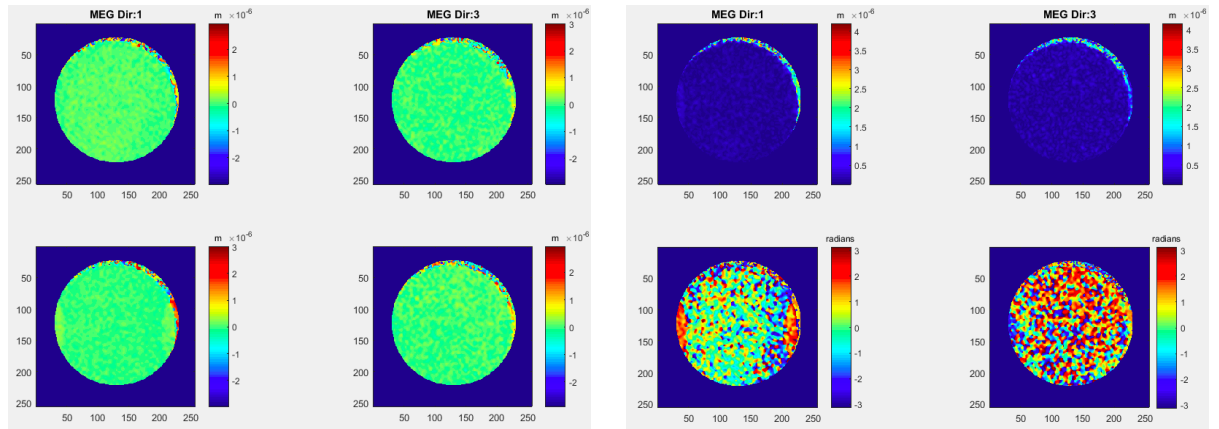


Figure 29: Waves images for 200Hz. On the left, top row: real part and top bottom: Imaginary part. On the right, top row: absolute values and top bottom: phase values

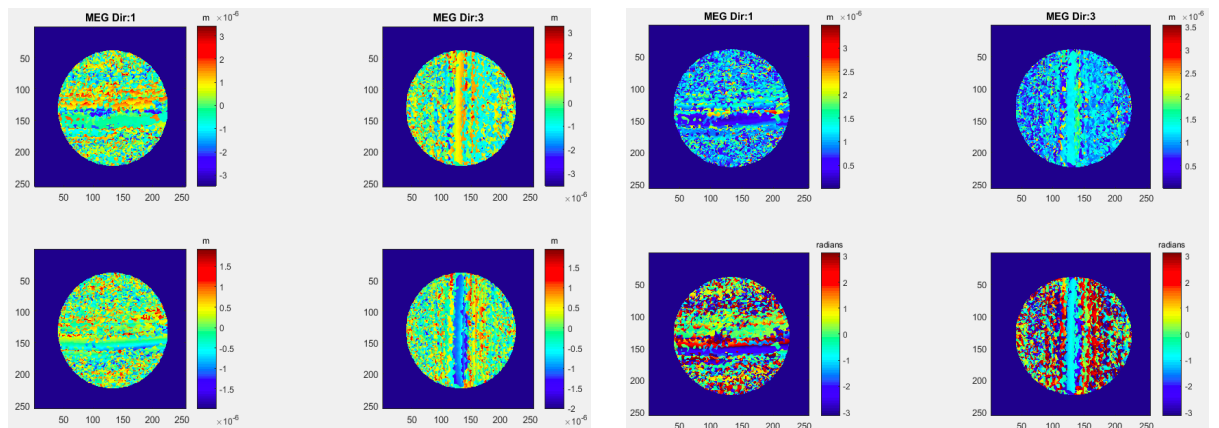


Figure 30: Waves images for 400Hz. On the left, top row: real part and top bottom: Imaginary part. On the right, top row: absolute values and top bottom: phase values

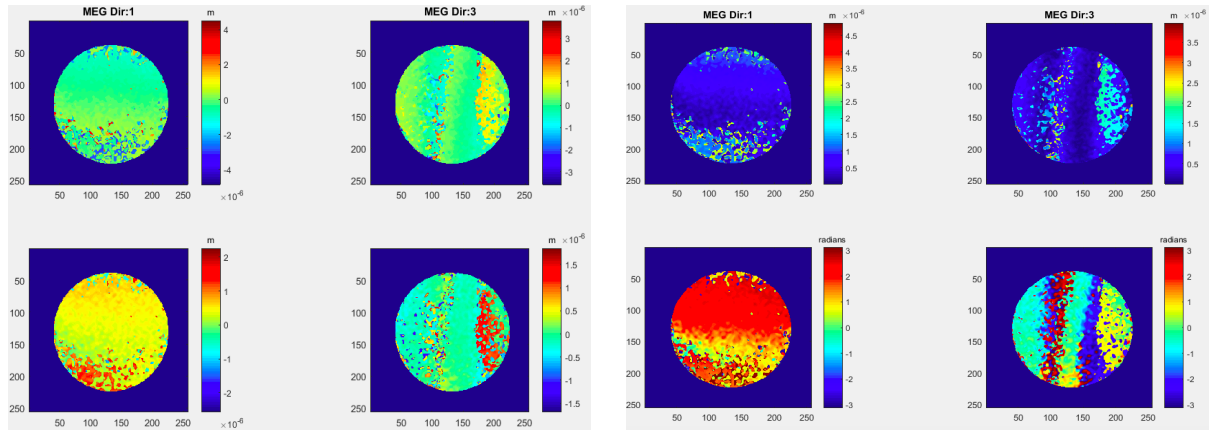


Figure 31: Waves images for 600Hz. On the left, top row: real part and top bottom: Imaginary part. On the right, top row: absolute values and top bottom: phase values

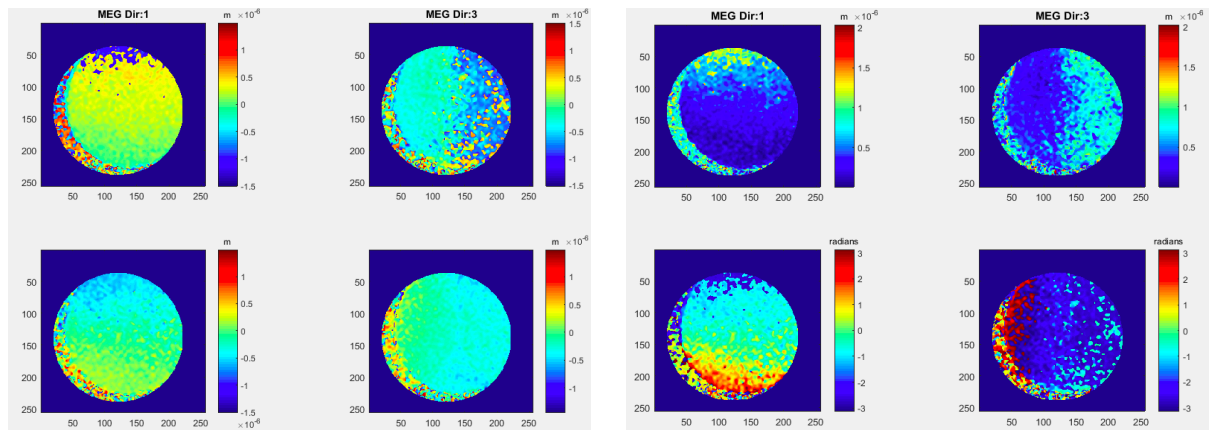


Figure 32: Waves images for 800Hz. On the left, top row: real part and top bottom: Imaginary part. On the right, top row: absolute values and top bottom: phase values

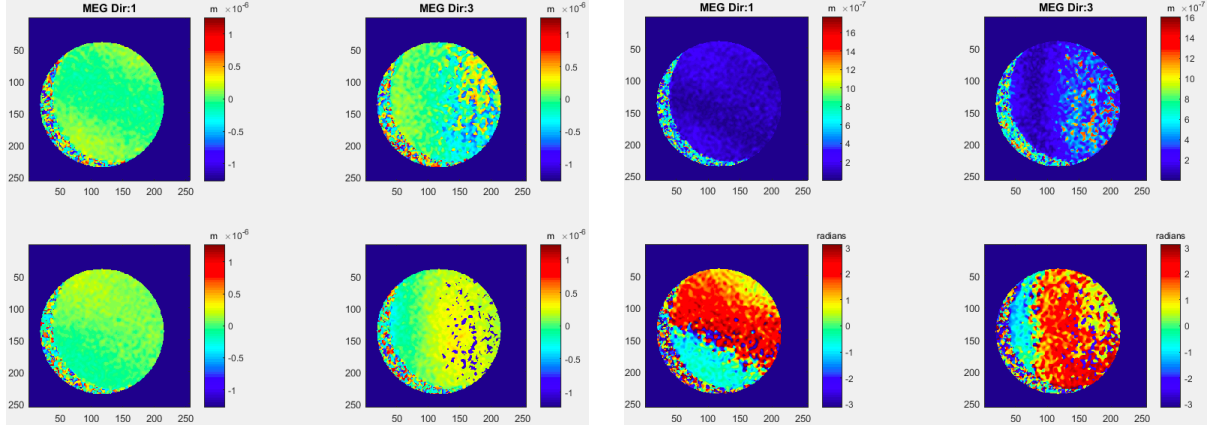


Figure 33: Waves images for 1000Hz. On the left, top row: real part and top bottom: Imaginary part. On the right, top row: absolute values and top bottom: phase values

As already mentioned, MRE sequence is characterized by the sequence diagram typical of the MRI with the addition of the vibration and the motion encoding gradient. This can be done for various acquisitions, because in MRE the acquisition is not just a snapshot of the mechanical wave, but there is the possibility to acquire multiple images at different time points.

The time points depend on the number of frequencies used: the higher the number of acquisitions, the easier to filter out higher frequency noise after applying the Discrete Fourier Transform. In general, 4 or 8 time steps are used.

Therefore, to better understand the meaning of the images, both magnitude and phase at each time instance were obtained. In this specific case, the time steps correspond to 8.

In Figure 34 and Figure 35 are showed the magnitude and phase of the mechanical waves for

400Hz, respectively. In Figure 36 and Figure 37 are represented the magnitude and phase images for 600Hz, respectively.

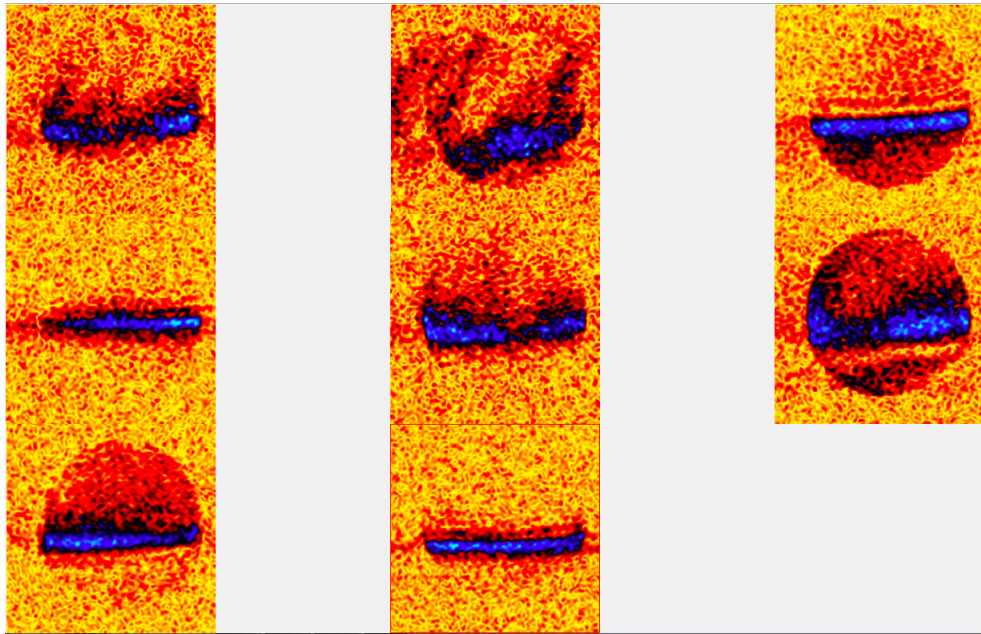


Figure 34: Magnitude images for each time steps at 400Hz.

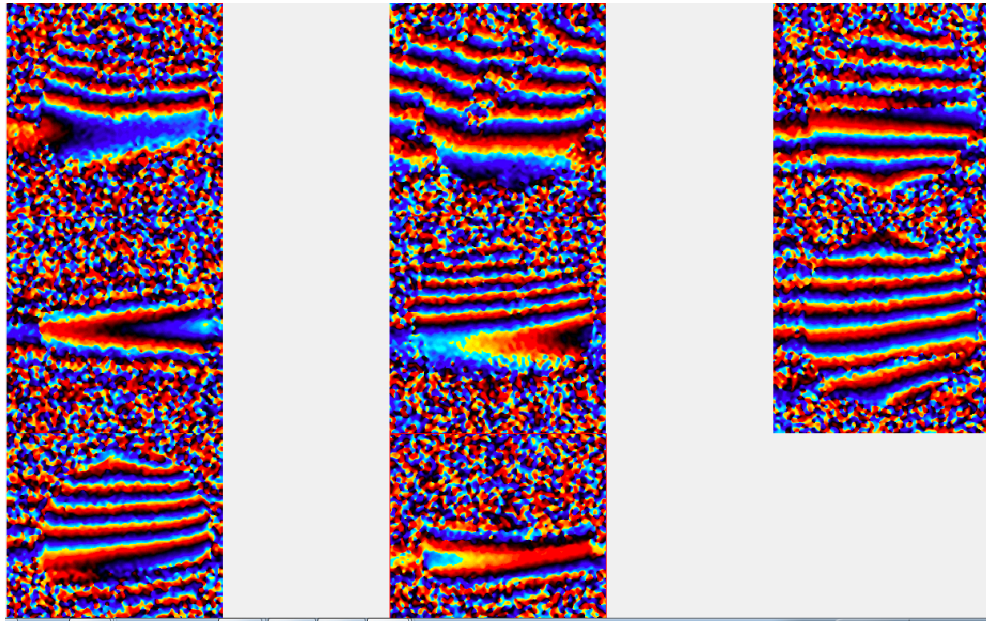


Figure 35: Phase images for each time steps at 400Hz.

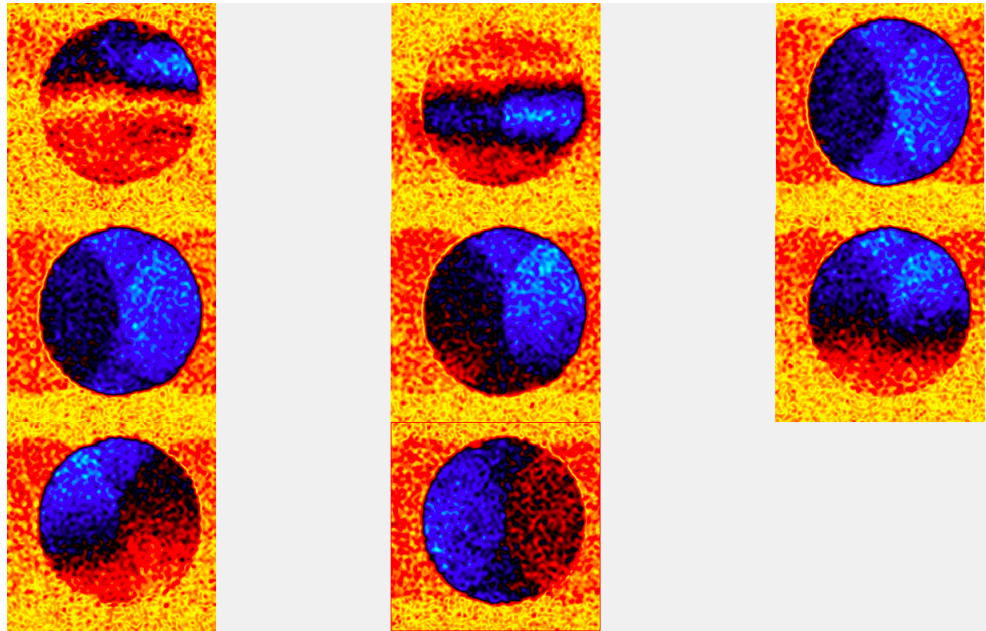


Figure 36: Magnitude images for each time steps at 600Hz.

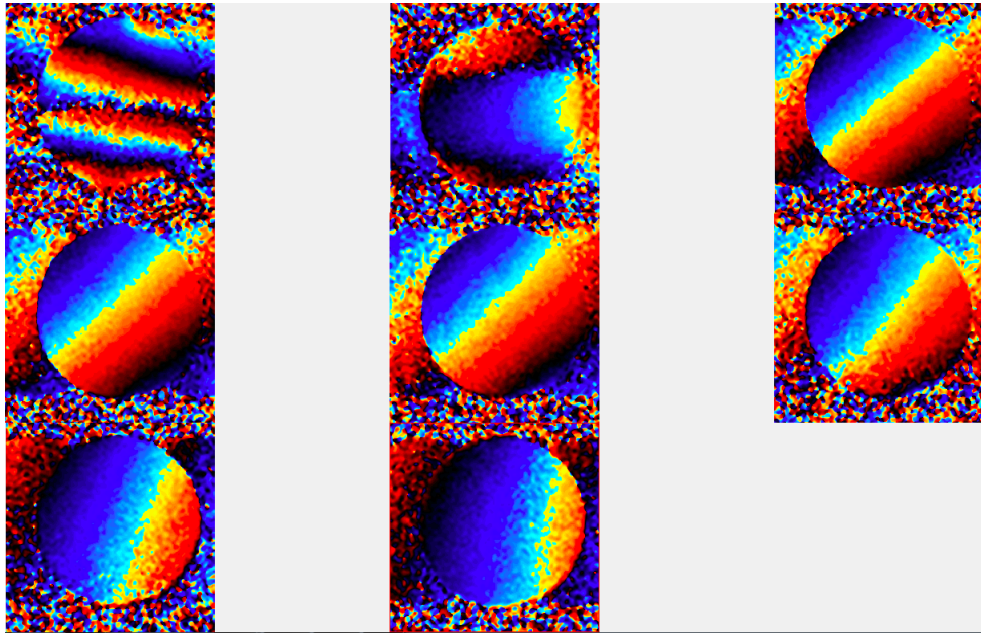


Figure 37: Phase images for each time steps at 600Hz.

Motion is detected for both 400Hz and 600Hz. In particular, for 400Hz the magnitude is characterized by a lot of vibrations, but the motion of the displacement is coherent with the direction of motion encoding. This means that the energy used during the experiment should be reduced.

Regarding the magnitude at 600Hz, at the first time step there is motion coherent with the motion encoding direction. From the second to the last one instead, it seems that a problem with the actuator was detected, and for this reason there is no motion transmitted to the phantom. A lot of phase wraps are present in the phase images, an unwrapping algorithm was used to

remove phase wraps, but on some images it was not possible to remove them.

6.2.2.1 Excitation with prestrains

The setup was also analyzed by elongating the phantom by 10% and 20% of its initial length with the lead weights, using the anchor attached to the phantom, as showed in Figure 38.

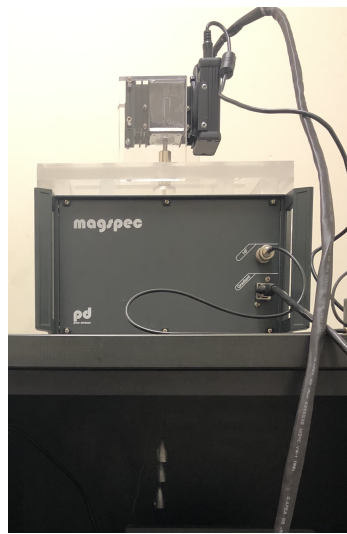


Figure 38: Stepper Motor Setup with the weights for a 10% prestrain.

The motion has been analyzed for the same range of frequency from 200 to 1000Hz, with a 10% elongation from the initial length of the phantom. In Figure 42 are illustrated the wave images in the x and z direction for 400 Hz and 800 Hz.

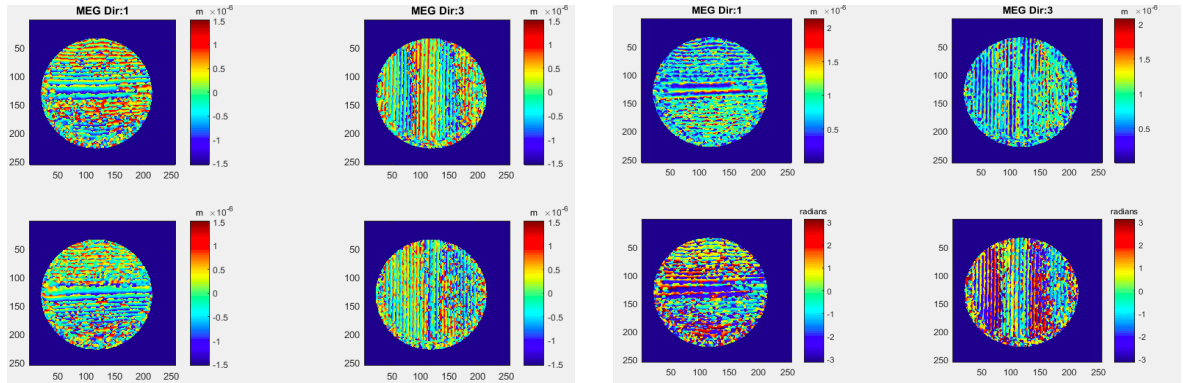


Figure 39: Waves images for 400Hz. On the left, top row: real part and top bottom: Imaginary part. On the right, top row: absolute values and top bottom: phase values

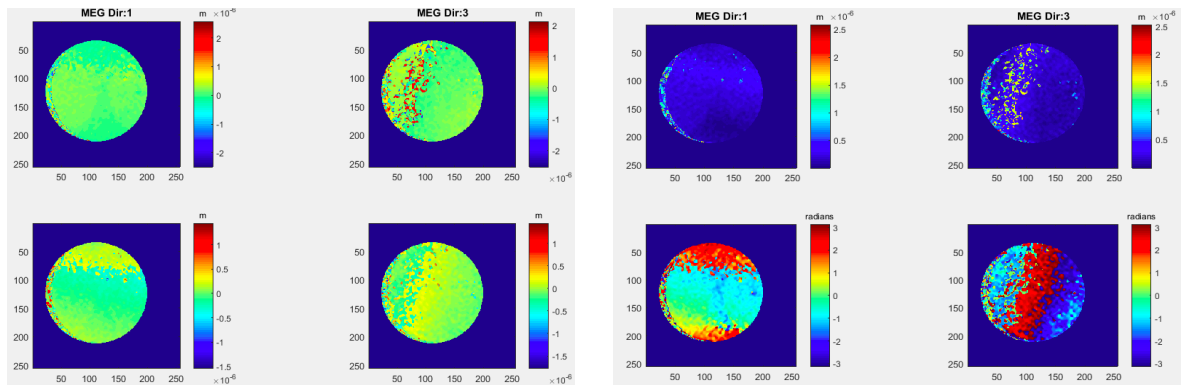


Figure 40: Waves images for 800Hz. On the left, top row: real part and top bottom: Imaginary part. On the right, top row: absolute values and top bottom: phase values

Then, the phantom has been analyzed for 20% elongation. The results gained are pictured in Figure 41 and Figure 42

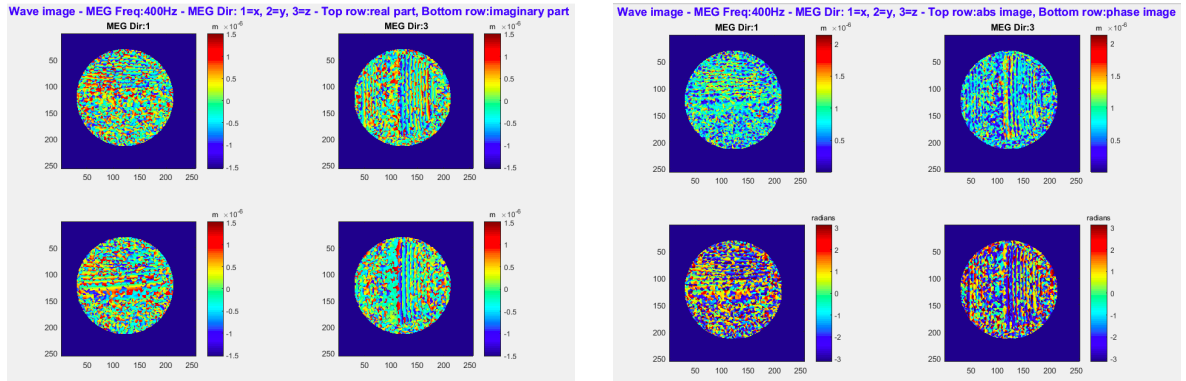


Figure 41: Waves images for 400Hz. On the left, top row: real part and top bottom: Imaginary part. On the right, top row: absolute values and top bottom: phase values

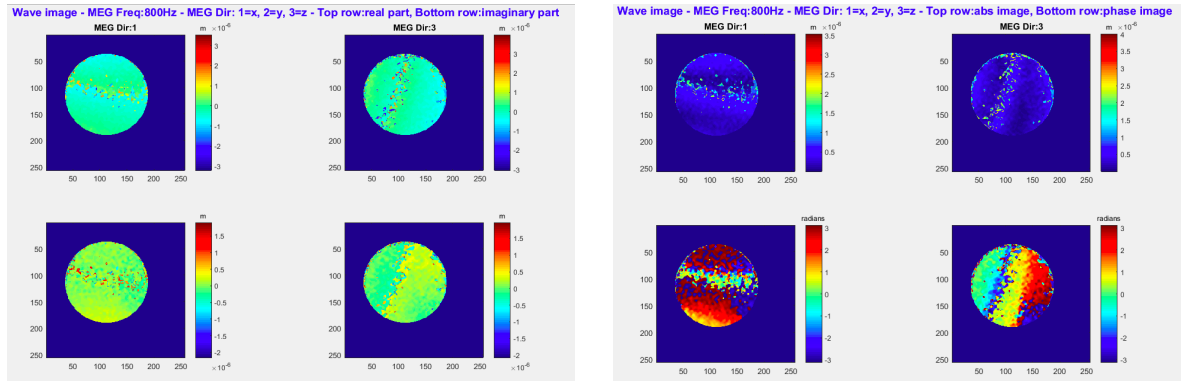


Figure 42: Waves images for 800Hz. On the left, top row: real part and top bottom: Imaginary part. On the right, top row: absolute values and top bottom: phase values

In this case, the diameter of the phantom is reduced, because of the application of the weights.

6.3 COMSOL analysis

To validate and get a better understanding of the experimental results, a comparison with the computational study has been made.

The results represent the absolute value of the wave images in the x and z direction of the axial slices of the phantom, such that they could be compared with the setup, and of the sagittal slices to better understand how the mechanical waves propagate through the whole phantom. In addition, as a consequence of the experimental results it was analyzed also the axial displacement for both axial and sagittal slice.

The experiments are done for 200Hz, 400Hz, 600Hz, 800Hz and 1000Hz.

Regarding the axial displacement, results are showed in Figure 43, Figure 44, Figure 45 and Figure 46. The above mentioned images depict the axial and sagittal slices in both the x and z direction for 400Hz at 0%, 10% and 20% elongation.

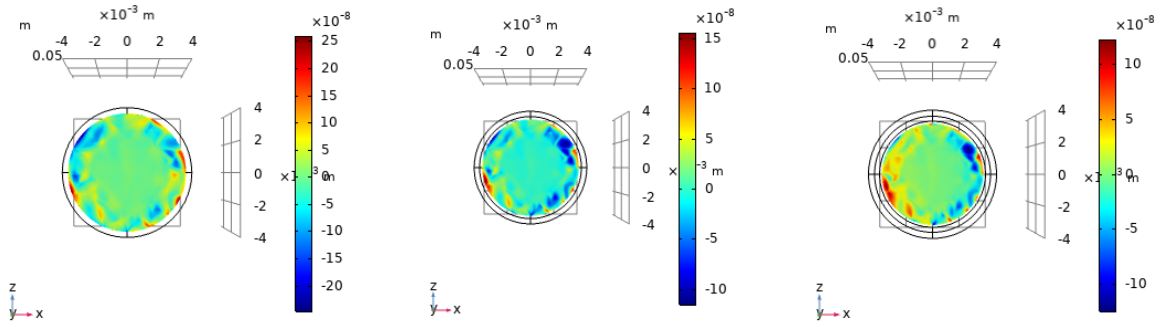


Figure 43: From the left to the right: axial slices in the x-direction of wave images for 0%, 10% and 20% elongation for 400Hz.

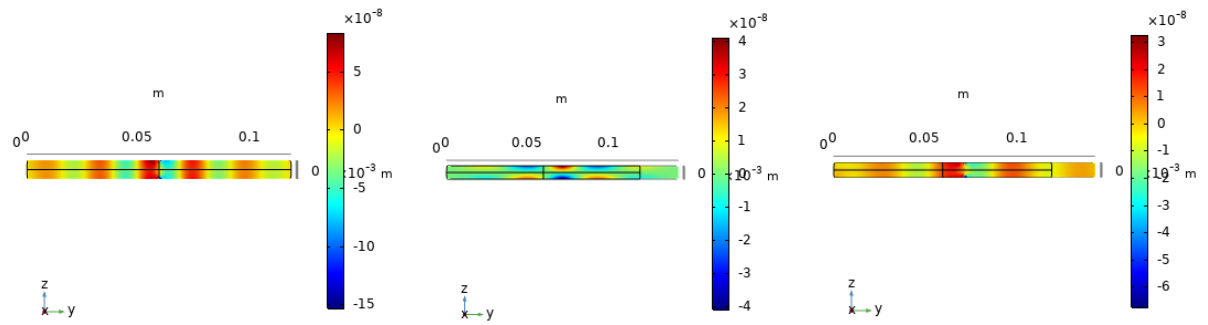


Figure 44: From the left to the right: axial slices in the z-direction of wave images for 0%, 10% and 20% elongation for 400Hz.

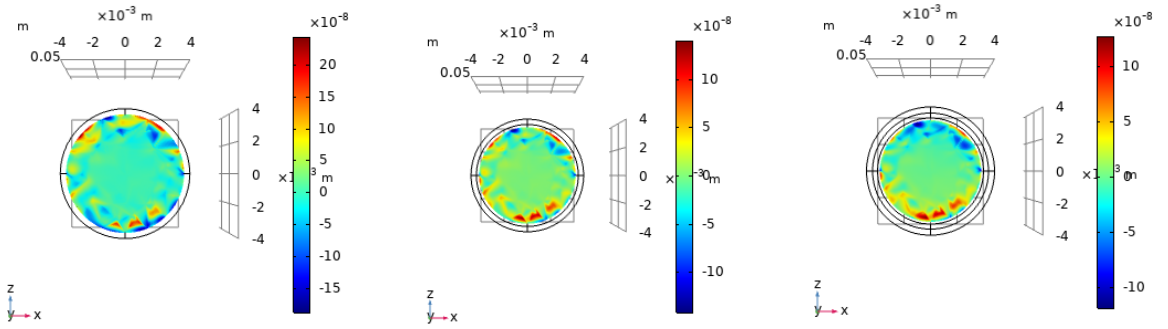


Figure 45: From the left to the right: axial slices in the z -direction of wave images for 0%, 10% and 20% elongation for 400Hz.

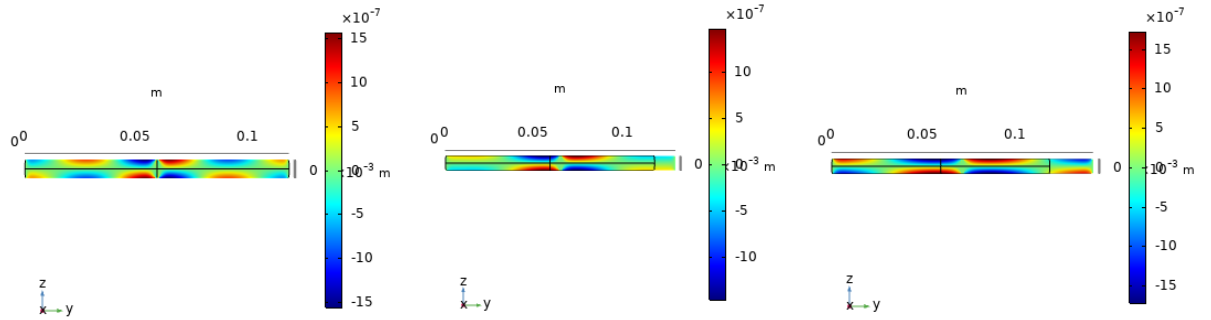


Figure 46: From the left to the right: axial slices in the z -direction of wave images for 0%, 10% and 20% elongation for 400Hz.

For torsionally-polarized excitation we'd want to have a sagittal slice in the x-y plane with motion encoded in the z direction, or a slice in the z-y plane with motion encoded in the x direction.

The results gained by applying a torsional vibration instead, are showed in Figure 47, Figure 48, Figure 49 and Figure 50, depicting the axial and sagittal slices in both the x and z direction for 400Hz at 0%, 10% and 20% elongation.

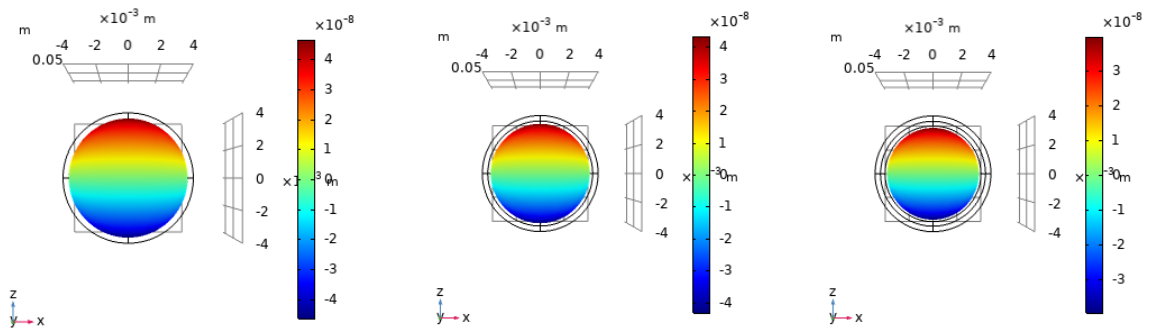


Figure 47: From the left to the right: axial slices in the x-direction of wave images for 0%, 10% and 20% elongation for 400Hz.

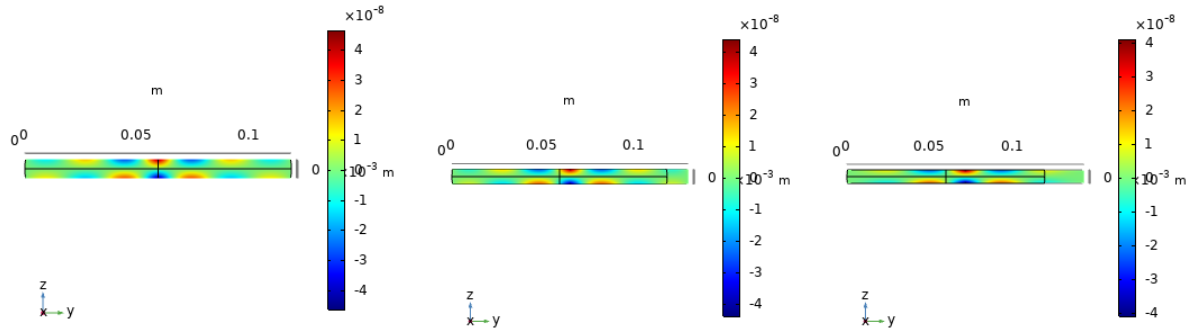


Figure 48: From the left to the right: sagittal slices in the x-direction of wave images for 0%, 10% and 20% elongation for 400Hz.

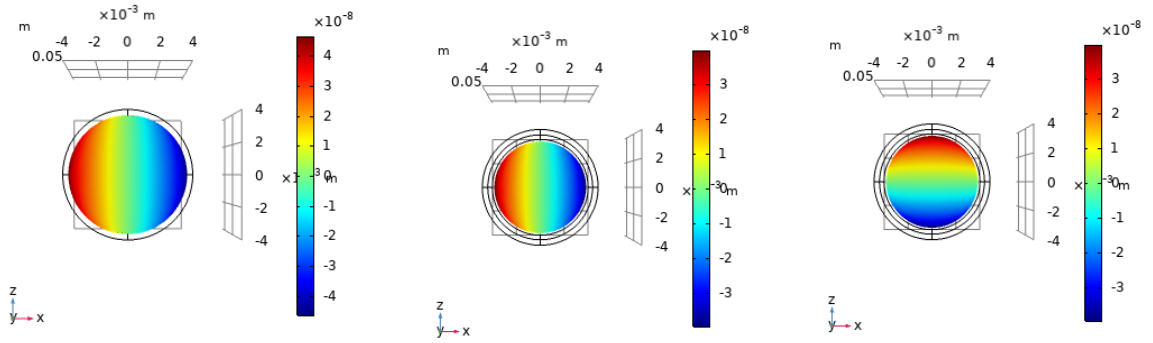


Figure 49: From the left to the right: axial slices in the z-direction of wave images for 0%, 10% and 20% elongation for 400Hz.

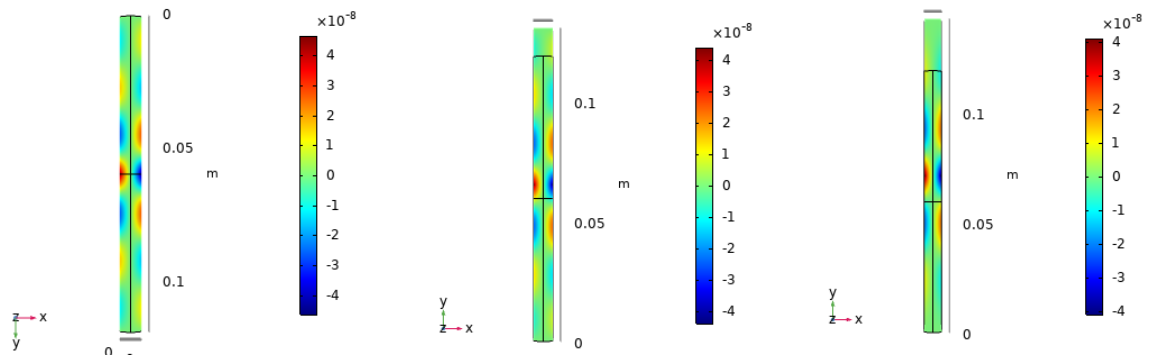


Figure 50: From the left to the right: sagittal slices in the z-direction of wave images for 0%, 10% and 20% elongation for 400Hz.

CHAPTER 7

CONCLUSION

The aim of this research study was to design and test a new experimental configuration to generate and measure torsionally-polarized and axially-polarized radially-converging shear wave motion in a cylindrcially shaped soft tissue phantom under varying axial tensile pres-stress conditions.

This involved developing a new tissue phantom fixture that allowed for controlled simultaneous tensile pre-stress and a new mechanism for torsional excitation to improve upon the bandwidth limitation of the current stepper motor configuration.

The planned experimental approach also was computationally simulated using finite element analysis (FEA) to gain insight into how different parameters affect the generated shear wave field in the phantom.

The torisonally-polarized motion detection can be broken down into two Cartesian directions in the tabletop MRI system, the x (1) direction and the z (3) direction. Initial motion encoding measurements in these directions using the stepper motor have identified some challenges associated with the new phantom configuration. Slight eccentricity in the phantom geometry or how it's affixed to torsional driver can result in rocking or other types of non-torsional motion that will need to be reduced and/or filtered out to improved measurement capability.

Additionally, the vibration was not sufficiently transmitted to the phantom at higher frequencies of interest, because of low resonance frequency of the system. For this reason, a new setup

was designed consisting of two piezoelectric actuators with the aim to improve the transmission of torsional vibration to the phantom, to gain better wave images and to eliminate or improve the noise; while the design of this new system is complete, delay on shipment of one necessary component has meant that it cannot be evaluated experimentally.

There are some improvements and considerations that can be made in this study. First of all, in order to understand better the behaviour of the phantom during torsional excitation more experiments and analysis should be done. The acquisition of the images of the mechanical waves needs improvement as noted above.

Also, in this study *Ecoflex*TM 00-30 was used, but in future studies it would be useful and important to analyse lower stiffness phantom materials, such as *Ecoflex*TM 00-20, since it may be closer to biological soft tissue properties.

Further analysis, should focus also on anisotropic phantoms, in order to mimic in a better way the mechanical properties of, for example, striated muscle tissue and brain white matter. Finally, once the new setup is validated for transmitting torsional vibration, few upgrades can be made in its design. For example, a better means of coupling the specimen, whether it be a phantom or excised biological tissue, to the actuator could improve measurements. For soft tissue specimens a alternate way of securing an anchor to the tissue is needed to stretch it for tensile loading. For any design improvements one must remember to utilize only non magnetic components and to keep in consideration the design constraint of fitting things within the 10 mm vertical bore of the tabletop MRI.

APPENDICES

Appendix A

TECHNICAL DATA OF ACTUATORS

In this appendix, it is presented the datasheets and the technical drawings of the actuators used for the present work.

Appendix A (continued)



Piezo High Load Actuators

Technical data

series PAHL	unit	PAHL 18/20	PAHL 40/20	PAHL 60/20	PAHL 80/20	PAHL 100/20	PAHL 120/20	PAHL 140/20	PAHL 160/20	PAHL 180/20	PAHL 200/20
part. no.		P-171-00	P-172-00	P-173-00	P-174-00	P-175-00	P-176-00	P-177-00	P-178-00	P-179-00	P-180-00
motion (-10/+20%)*	µm	21	42	63	84	105	125	145	165	180	200
capacitance (±20%)**	µF	7	14	21	28	35	42	50.4	56	63	70
resolution***	nm	0.04	0.08	0.13	0.17	0.2	0.25	0.29	0.33	0.36	0.4
resonant frequency	kHz	22	12	8	6	5	4	3	3	3	2
stiffness	N/µm	165	83	55	41	33	28	24	21	19	17
blocking force	N	3500	3500	3500	3500	3500	3500	3500	3500	3500	3500
pre-load	N	350	350	350	350	350	350	350	350	350	350
operating voltage	V	-20...+130									
connector	voltage	- LEMO OS.302									
cable length	m	1									
dimensions	length L	mm	36	54	72	90	108	126	144	162	180
	diameter D	mm	20	20	20	20	20	20	20	20	20
series PAHL with spherical end R 2,5	unit	PAHL 18/20 R 2,5	PAHL 40/20 R 2,5	PAHL 60/20 R 2,5	PAHL 80/20 R 2,5	PAHL 100/20 R 2,5	PAHL 120/20 R 2,5	PAHL 140/20 R 2,5	PAHL 160/20 R 2,5	PAHL 180/20 R 2,5	PAHL 200/20 R 2,5
part. no.		P-171-50	P-172-50	P-173-50	P-174-50	P-175-50	P-176-50	P-177-50	P-178-50	P-179-50	P-180-50
dimensions	length L	mm	38.5	56.5	74.5	92.5	110.5	128.5	146.5	164.5	182.5
series PA SG with integrated measurement system	unit	PAHL 18/20 SG	PAHL 40/20 SG	PAHL 60/20 SG	PAHL 80/20 SG	PAHL 100/20 SG	PAHL 120/20 SG	PAHL 140/20 SG	PAHL 160/20 SG	PAHL 180/20 SG	PAHL 200/20 SG
part. no.		P-171-01	P-172-01	P-173-01	P-174-01	P-175-01	P-176-01	P-177-01	P-178-01	P-179-01	P-180-01
motion (±0.2%)* closed loop	µm	17	34	50	67	84	100	116	132	144	160
integrated measurement system		strain gage									
resolution closed loop	nm	0.4	0.8	1.2	1.6	2.0	2.4	2.8	3.2	3.6	4.0
typ. repeatability	nm	6	8	12	15	20	21	21	21	24	32
dimensions	length L	mm	40	58	76	94	112	130	148	166	184
series PA SG with integrated measurement system spherical end R 2,5	unit	PAHL 18/20 SG R 2,5	PAHL 40/20 SG R 2,5	PAHL 60/20 SG R 2,5	PAHL 80/20 SG R 2,5	PAHL 100/20 SG R 2,5	PAHL 120/20 SG R 2,5	PAHL 140/20 SG R 2,5	PAHL 160/20 SG R 2,5	PAHL 180/20 SG R 2,5	PAHL 200/20 SG R 2,5
part. no.		P-171-51	P-172-51	P-173-51	P-174-51	P-175-51	P-176-51	P-177-51	P-178-51	P-179-51	P-180-51
dimensions	length L	mm	42.5	60.5	78.5	96.5	114.5	132.5	150.5	168.5	186.5

* typical value measured with NV 40/3(closed loop NV 40/3 CLE)

** typical value for small electrical field strength



Tel: +49 (3641) 66880 • Fax: +49 (3641) 668866
info@piezsystem.com • www.piezsystem.com
 Series_PAHL_ds_Rev06_2014_07_10.doc

Figure 51: Datasheet of the Piezoelectric actuator 60/20

Appendix A (continued)

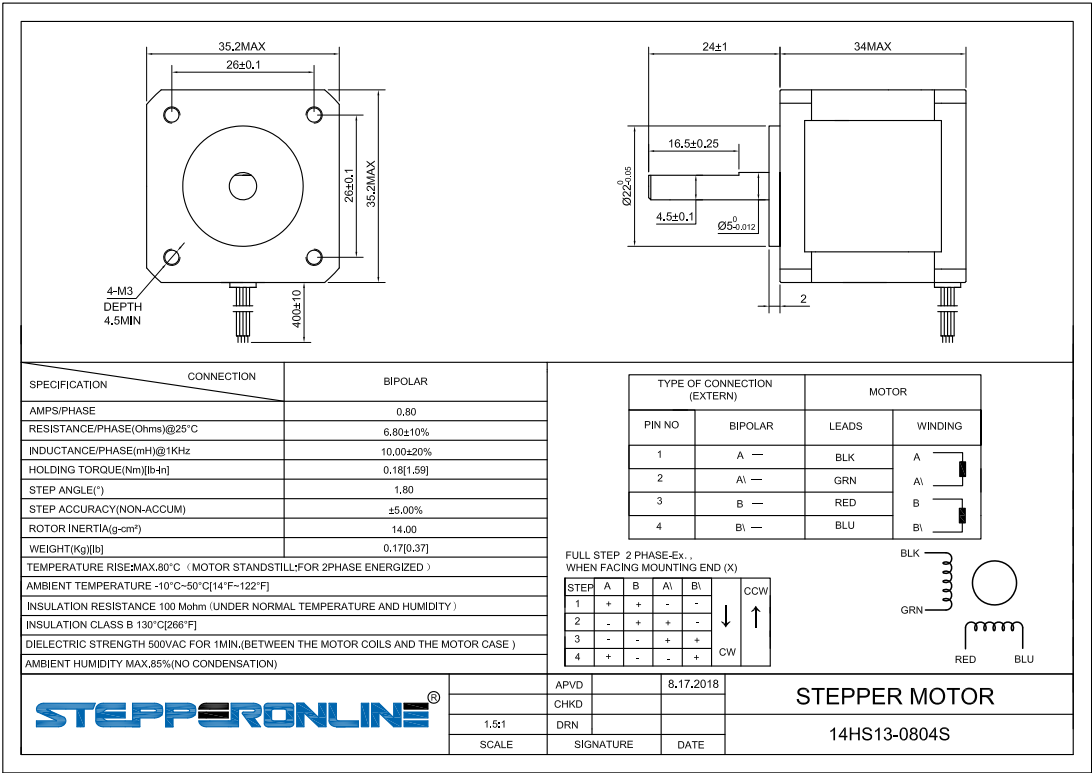


Figure 52: Datasheet of the Stepper Motor 14HS13-0804S

Appendix A (continued)



Specifications

	P-843.10	P-843.20	P-843.30	P-843.40	P-843.60	Unit	Tolerance
Travel range at 0 to 100 V	15	30	45	60	90	μm	
Sensor*	SGS	SGS	SGS	SGS	SGS		
Resolution**	0.3	0.6	0.9	1.2	1.8	nm	
Static large-signal stiffness***	57	27	19	15	10	N/μm	±20 %
Push force capacity	800	800	800	800	800	N	
Pull force capacity	300	300	300	300	300	N	
Torque on tip	0.35	0.35	0.35	0.35	0.35	Nm	max.
Electrical capacitance	1.5	3	4.5	6	9	μF	±20 %
Resonant frequency f_0 (no load)	18	14	10	8.5	6	kHz	±20 %
Operating temperature range	-40 to 80	-40 to 80	-40 to 80	-40 to 80	-40 to 80	°C	
Mass without cable	31	42	53	64	86	g	±5 %
Length	37	55	73	91	127	mm	
Recommended electronics	E-503, E-505, E-610, E-617, E-621, E-625, E-663, E-709, E-831	E-503, E-505, E-610, E-617, E-621, E-625, E-663, E-709, E-831	E-503, E-505, E-610, E-617, E-621, E-625, E-663, E-709, E-831	E-503, E-505, E-610, E-617, E-621, E-625, E-663, E-709, E-831	E-503, E-505, E-610, E-617, E-621, E-625, E-663, E-709, E-831		

* Models with SGS allow closed loop linearity up to 0.15 % and are shipped with performance reports.

** The resolution of the system is only limited by the noise of the amplifier and measuring technology because PI piezo actuators are free of friction.

*** Dynamic small-signal stiffness is approx. 30 % higher.

Voltage connection: LEMO FFA.00.250. Coaxial cable RG 178, 1 m.

Sensor connection: LEMO FFA.05.304. Cable, 1 m.

Housing / tip material: Stainless steel.

Vacuum versions to 10^{-6} hPa are available under the following ordering number: P-843.x0V.

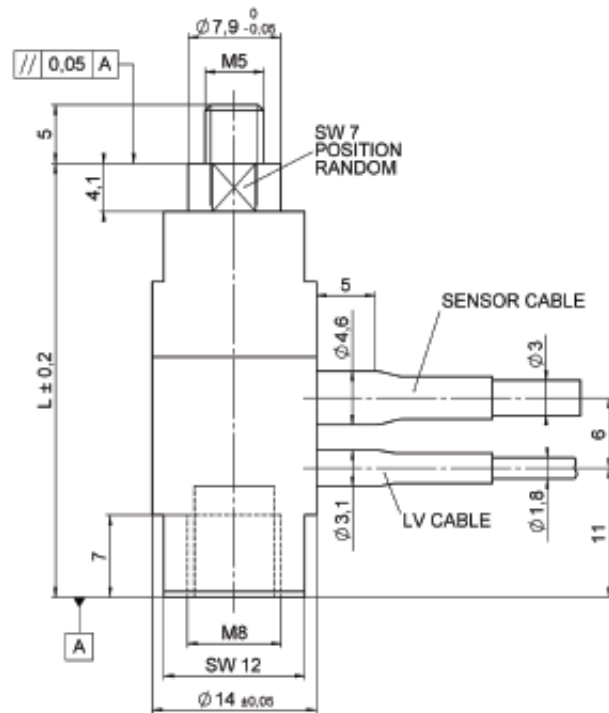
All specifications based on room temperature (22 °C ±3 °C).

26.10.2018

WWW.PI.WS

Figure 53: Datasheet of the Piezoelectric P842.10

Appendix A (continued)

PI**Drawings / Images**

Model	Travel range	L
P-842.10 / P-843.10	15 μm	37 mm
P-842.20 / P-843.20	30 μm	55 mm
P-842.30 / P-843.30	45 μm	73 mm
P-842.40 / P-843.40	60 μm	91 mm
P-842.60 / P-843.60	90 μm	127 mm

P-842 / P-843, dimensions in mm. Sensor included only with P-843.

25.10.2018

WWW.PI.WS

Figure 54: Technical Drawing of the Piezoelectric P842.10

Appendix A (continued)

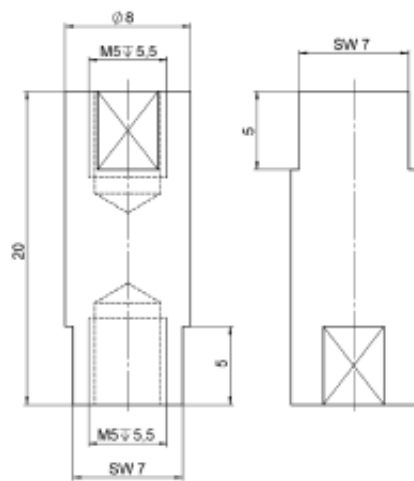
PI**Drawings / Images***P-176.50, dimensions in mm*

Figure 55: Datasheet and technical drawing of the flexible tip P176.50

CITED LITERATURE

1. Yogesh K. Mariappan, Kevin J. Glaser, a. R. L. E.: Magnetic resonance elastography: A review. Clinical Anatomy, 23(5):497–511, 2010.
2. Liver biopsy. <https://www.mayoclinic.org/tests-procedures/liver-biopsy/about/pac-20394576>. Accessed: 2021-03-03.
3. Rosa M.S. Sigrist¹, Joy Liau¹, A. E. K. M. C. C. J. K. W.: Ultrasound elastography: Review of techniques and clinical applications. Theranostics, 7(5):1303–1329, 2014.
4. Ehman, S. K. V. R. L.: Magnetic Resonance Elastography, chapter 1. Springer, 2014.
5. Sebastian Hirsch, J. B. and Sack, I.: Magnetic Resonance Elastography Physical Background and Medical Applications, chapter 6.1. Wiley-VCH, 2017.
6. Zampini, M. A.: 0.5T Benchtop Magnet: Development of a MR Elastography Setup and Tissue Samples Characterization. Thesis, University of Illinois at Chicago, 2018.
7. Matt A. Bernstein, K. F. K. and Zhou, X. J.: Handbook of MRI Pulse Sequences, chapter 9. Elsevier, 2004.
8. Lecture notes, bioe 594 "elastography", instructor: Dieter klatt, fall 2020, university of illinois at chicago. Accessed: 2021-04-21.
9. Flip (or tip) angle. <http://mriquestions.com/what-is-flip-angle.html>. Accessed: 2021-03-06.
10. Magnetic resonance imaging (mri) of the brain and spine: Basics. <https://case.edu/med/neurology/NR/MRI%20Basics.htm>. Accessed: 2021-03-06.
11. Basics of magnetic resonance imaging. <https://cfmi.georgetown.edu/downloads/training/2/MRI-basics.pdf>. Accessed: 2021-03-05.
12. Pautler, R. G.: Mouse mri: Concepts and applications in physiology. Physiology, 19:168–175, 2004.

CITED LITERATURE (continued)

13. Sebastian Hirsch, J. B. and Sack, I.: Magnetic Resonance Elastography Physical Background and Medical Applications, chapter 12.5. Wiley-VCH, 2017.
14. Meng Yin, Armando Manduca, R. C. G.: Liver magnetic resonance elastography technique. Magnetic Resonance Elastography, pages 19–37, 2014.
15. Christopher L. Farrow, Margaret Shaw, H. K. P. J. and Billinge, S. J.: Nyquist-shannon sampling theorem applied to refinements of the atomic pair distribution function. physical review B, 84:134105, 2011.
16. Guidetti, M.: Transverse Isotropic Multiscale Muscle Phantom for MR Elastography. Thesis, University of Illinois at Chicago, 2016.
17. Body waves. body waves include p-waves and s-waves. <http://www.seismicresilience.org.nz/topics/seismic-science-and-site-influences/earthquake-energy/body-waves/>. Accessed: 2021-03-08.
18. Graff, K. F.: Wave Motion in Elastic Solids, chapter 6.1.4. Oxford University Press, London (Clarendon Press, Oxford), 1991.
19. Longitudinal and transverse wave motion. <https://www.acs.psu.edu/drussell/Demos/waves/wavemotion.html>. Accessed: 2021-03-08.
20. Travis E. Oliphant, Armando Manduca, R. L. E. and Greenleaf, J. F.: Complex-valued stiffness reconstruction for magnetic resonance elastography by algebraic inversion of the differential equation. Magnetic Resonance in Medicine, 45:299–310, 2001.
21. DJ Tweten, R. O. and Bayly, P.: Requirements for accurate estimation of anisotropic material parameters by magnetic resonance elastography: A computational study. Magnetic Resonance in Medicine, 78(6):2360–2372, 2017.
22. Jin Long Yue, Marion Tardieu, F. J. T. B. R. S. C. P.-B. X. M.: Acquisition and reconstruction conditions in silico for accurate and precise magnetic resonance elastography. Physics in Medicine and Biology, 62(22):8655–8670, 2017.
23. Sebastian Hirsch, J. B. and Sack, I.: Magnetic Resonance Elastography Physical Background and Medical Applications, chapter 10. Wiley-VCH, 2017.

CITED LITERATURE (continued)

24. Joaquin Mura, F. S. and Sack, I.: An analytical solution to the dispersion-by-inversion problem in magnetic resonance elastography. Magnetic Resonance in Medicine, 00:1–11, 2020.
25. A. Manduca, T.E. Oliphant, M. D. J. M. S. K. E. A. J. F. J. G. R. E.: Magnetic resonance elastography: Non-invasive mapping of tissue elasticity. Medical Image Analysis, 5:237–254, 2001.
26. Howard Anton, C. R.: Elementary Linear Algebra, chapter 1. John Wiley Sons, 2005.
27. Sebastian Hirsch, J. B. and Sack, I.: Magnetic Resonance Elastography Physical Background and Medical Applications, chapter 10.3. Wiley-VCH, 2017.
28. Liu, C.-S. and Chang, C.-W.: A real-time lie-group differential algebraic equations method to solve the inverse nonlinear vibration problems. Inverse Problems in Science and Engineering, 24:1569–1586, 2016.
29. Sebastian Hirsch, J. B. and Sack, I.: Magnetic Resonance Elastography Physical Background and Medical Applications, chapter 10.1. Wiley-VCH, 2017.
30. S Papazoglou, U Hamhaber, J. B. and Sack, I.: Algebraic helmholtz inversion in planar magnetic resonance elastography. PHYSICS IN MEDICINE AND BIOLOGY, 53:3147—3158, 2008.
31. Ochala, W. R. F. J.: Skeletal muscle: A brief review of structure and function. Calcif Tissue Int, 96:183—195, 2014.
32. Wolfe, R. R.: The underappreciated role of muscle in health and disease. The American Journal of Clinical Nutrition, 84:475–482, 2006.
33. Hikida, R. S.: Aging changes in satellite cells and their functions. Curr Aging Sci, 4:279–297, 2011.
34. Structure of skeletal muscle. <https://www.training.seer.cancer.gov/anatomy/muscular/structure.html>. Accessed: 2021-03-15.
35. RDuane A. Morrow, MS, T. L. H. D. P. G. M. O. and Kenton R. Kaufman, PhD, P.: Transversely isotropic tensile material properties of skeletal muscle tissue. J Mech Behav Biomed Mater., 3(1):124—129, 2010.

CITED LITERATURE (continued)

36. Sebastian Papazoglou, Jürgen Braun, U. H. and Sack, I.: Two-dimensional waveform analysis in mr elastography of skeletal muscles. Phys. Med. Biol., 50:1313—1325, 2005.
37. R Sinkus¹, M Tanter, S. C. J. L. C. K. E. S. M. F.: Imaging anisotropic and viscous properties of breast tissue by magnetic resonance-elastography. Magn Reson Med., 53(2):372–387, 2005.
38. Guidetti, M. and Royston, T. J.: Analytical solution for converging elliptic shear wave in a bounded transverse isotropic viscoelastic material with nonhomogeneous outer boundary. P2018 Acoustical Society of America, 144:2312–2323, 2018.
39. Dieter Klatt, Uwe Hamhaber, P. A. J. B. and Sack, I.: Noninvasive assessment of the rheological behavior of human organs using multifrequency mr elastography: a study of brain and liver viscoelasticity. Physics in Medicine and Biology, 52:7281–7294, 2007.
40. Temel K. Yasar, T. J. R. and Magin, R. L.: Wideband mr elastography for viscoelasticity model identification. Magnetic Resonance in Medicine, 70(2):479–489, 2012.
41. Chiara, G.: Multimodal Actuation in Magnetic Resonance Elastography Experiments. Thesis, University of Illinois at Chicago, 2020.
42. Instructional tabletop mri scanner. <https://www.opensourceimaging.org/project/instructional-tabletop-mri-scanner/>. Accessed: 2021-03-28.
43. Benchtop mri spectrometers - pure devices. <https://www.pure-devices.com>. Accessed: 2021-03-28.
44. Benchtop mri spectrometers - pure devices. https://tabletop.martinos.org/index.php/Main_Page. Accessed: 2021-03-28.
45. Carla, F.: Mechanical and calorimetric characterization of novel environmentally friendly copolymers. phd thesis, Politecnico di Milano, 2014.
46. Magin, T. K. Y. T. J. R. R. L.: Wideband mr elastography for viscoelasticity model identification. Magnetic Resonance in Medicine, 70:479–489, 2012.
47. Pdv-100 portable digital vibrometer. <https://www.atecorp.com/atecorp/media/pdfs/data-sheets/polytec-pdv-100.pdf?ext=.pdf>. Accessed: 2021-04-05.

CITED LITERATURE (continued)

48. Chapter 3.3 laser doppler vibrometry. <http://www.science4heritage.org/COSTG7/booklet/chapters/ldv.htm>. Accessed: 2021-04-05.

VITA

NAME: Federica Dibennardo

EDUCATION: Bachelor of Science in Biomedical Engineering, Politecnico di Milano, Milan, Italy, 2016–2019

Master of Science in Biomedical Engineering, Politecnico di Milano, Milan, Italy, 2019–*Present*

Master of Science in Bioengineering, University of Illinois at Chicago, Chicago, 2019–*Present*

EXPERIENCE: Graduate Research Assistant in the Acoustics and Vibrations Laboratory, Richard and Loan Hill Department of Bioengineering, University of Illinois at Chicago, Chicago, Gen 2021–*Present*